Computers and Geotechnics 117 (2020) 103234

Contents lists available at ScienceDirect

Computers and Geotechnics

journal homepage: www.elsevier.com/locate/compgeo

Research Paper

Discontinuous deformation analysis for SH-body

Huo Fan[a], Duruo Huang[b,*], Gang Wang[a,*], Jianfeng Wang[c]

[a] Department of Civil and Environmental Engineering, The Hong Kong University of Science and Technology, Clear Water Bay, Kowloon, Hong Kong
[b] Department of Hydraulic Engineering, Tsinghua University, Beijing 100084, China
[c] Department of Architecture and Civil Engineering, City University of Hong Kong, Kowloon, Hong Kong

ARTICLE INFO

Keywords:
Spherical harmonic function
Surface reconstruction
Discontinuous deformation analysis
Geometric iteration
Variational inequality

ABSTRACT

Based on micro X-ray computed tomography data, the spherical harmonic (SH) function can be employed to reconstruct the nature sand particle, referred to as SH-body. Thus, the sand particle micromorphology can be described by analytic functions. Thanks to these analytic functions, the closest points between SH-bodies for contact detection can be identified by using a second-order geometric iteration algorithm. Meanwhile, the equivalent variational inequality is formulated to determine the inter-particle contact forces for the three-dimensional cases. To capture the kinematics and kinetics of SH-bodies, this study deduces discontinuous deformation analysis (DDA) formula based on the principle of minimum potential energy. The study establishes a framework for simulating the dynamic behavior of SH-bodies, and the proposed methodology is validated through numerical examples.

1. Introduction

Recently, researches have been rapidly developed to investigate origin, chemical components, physical properties, microstructures, and surface texture of granular materials. Particularly, the development and application of the micro X-ray computed tomography (μCT) [1–3] have greatly promoted the insight on the micromorphology of sand particle.

A typical procedure of acquiring μCT data contains the several steps: Scanning the specimen to obtain a series of X-ray adsorption images (i.e. projections, cross-sectional images, or slices) indicated by two-dimensional pixel [4]; Assembling these slices to produce corresponding stereoscopic digital image (or tomographic map) described by three-dimensional voxel [5]; Extracting spatial coordinates to generate geometry model (or reconstructed surface) [6]. Generally speaking, there mainly are several approaches to represent geometry of a reconstructed surface: *The first approach* is the triangular meshes, which is usually obtained from the marching cubes [7] on the basis of the tomographic map. The marching tetrahedrons [8] can be employed to correct some ambiguities in marching cubes. Moreover, Laplacian smoothing [9] and Gaussian filtering [10] can be utilized to eliminate the artificial stair-steps appearing the marching-type algorithms. *The second approach* is the level set [11,12], which is a real-valued implicit function whose value is the signed distance from a point to an interface. Specified that it is positive outside the particle and it is negative inside the same particle [13], one can obtain the discretized level set [14], which is the result of image segmentation by using the edge-based level set algorithm [15]. The particle surface is the set of all real-valued roots of an equation indicating the zero level set. Thus, the reconstructed surface is composed of a large number of discrete points. *The third method* is B-spline method [16]. The interpolation-type algorithm will generates an interpolating reconstructed surface that passes through the data points. While the approximation-type algorithm will leads to an approximating reconstructed surface that passes near the data points, minimizing the deviation of the surface from the data points [17]. Firstly, the approximations on some sub-domains are solved. Then, these approximations are blended by weight functions to build the global approximation [18]. However, how to insert the knots and choose the proper weight functions is still an open question [19]. And *the fourth approach* is the spherical harmonic (SH) functions [20]. Spherical harmonic functions are defined as the eigenfunctions of the angular part of the -Laplacian equation in spherical coordinates [21]. The spherical harmonics, the low-resolution spherical harmonics [22], and weighted spherical harmonics [23] have become a powerful tool in reconstructing the star-shaped objects [24–32]. In this study, this type of reconstructed surface is referred to as *SH-surface* and the corresponding body is called as *SH-body* that is regarded as rigid body.

In 2006, Li et al. [33] designed the so-called CLAD mapping algorithm that can control the length and area distortions simultaneously and that can enable the mapping operation work on the general triangular meshes no limited to the voxel data. Moreover, the open source

* Corresponding authors.
E-mail addresses: huangduruo@tsinghua.edu.cn (D. Huang), gwang@ust.hk (G. Wang).

https://doi.org/10.1016/j.compgeo.2019.103234
Received 14 June 2019; Received in revised form 28 August 2019; Accepted 29 August 2019

code SPHARM-MAT [34] makes the SH-based reconstruction easier to carry out. Based on these works, several SH-based descriptors were suggested [35,36] to quantify the micromorphology of sand particles and regenerate near-real sand particles statistically. In order to reveal the relationship between the macroscopic mechanical behaviors and the particle microscopic morphology, the capture of the motion of particles plays an important role especially the treatment of the contacts between particles. In the context of the SH-surface, the reconstructed surface is described explicitly by several analytic functions. However, the analytic properties of the reconstructed surface are still underutilized. On the other hand, discontinuous deformation analysis (DDA) had been generally recognized as a useful tool for describing the motion of discrete medium [37–41] and solving geotechnical engineering problems, such as the cohesive-frictional slope analysis [42], the dynamic response of sites containing discontinuities [43], the evaluation of impact force induced by rock landslides [44]. An explicit version of DDA [45] and a new joint definition [46] have been proposed. Most recently, parallel computing of DDA had also been implemented [47,48]. Nevertheless, to the best knowledge of the authors, the DDA framework accommodating complex morphology of particles or bodies has not been established.

To capture the interaction between SH-bodies carrying the information on nature bodies' shapes, in this study, from the view of the principle of minimum potential energy, we deduce the formula of DDA, in which the degree of freedoms and interpolation matrix are both independent of the geometry of particle. We extend the geometric iteration algorithms [49] to closed SH-surface to identify contacts among SH-bodies. To calculate the contact force, we generalize an equivalent variational inequality [50] to the three-dimensional setting, from which the resulting contact forces preserve momentum and energy [51]. Consequently, a DDA framework for simulating the dynamic behavior of SH-bodies is established. The presented methodology has a broad application in simulating interaction involving complex-shaped objects, which can be reconstructed by SH functions.

2. Description of particle surface by SH

Mathematically, a *star-shaped* object has at least one interior point that can connect any surface point with a line lying entirely within the particle. The surface of a star-shaped object can be entirely defined by a continuous function $r(\theta, \varphi)$, which is the radial distance from centre of particle to a point on the particle surface along the direction (θ, φ). The angles θ and φ are called polar and azimuthal angles, respectively, as shown in Fig. 1(a).

The micro X-ray computed tomography (μXCT) technology can be employed to acquire the cross-sectional images (or slices) of a star-shaped object, which can be further assembled (or stacked) into 3D images that is usually a 3D binary voxel data representing a particle surface. In general, 3D binary voxel data may contain some non-connective edges and vertices, or inherent internal voids. Obviously, the existence of these components will violate the continuity of the function $r(\theta, \varphi)$. Thus, before further analysis, they should be first identified and discarded. This study employs the "Topology Fix" tool of the open-source program SPHARM-MAT [34] to achieve this purpose, followed by the so-called spherical parameterization, through which the points on the original star-shaped object are mapped to the corresponding points on the unit sphere in the one-to-one manner. During the spherical parameterization, it is necessary to sample the spherical coordinates (θ, φ) from the unit sphere (see Fig. 1(a)), whose centre is taken as the origin, to set up the SH functions ($Y_n^m(\theta, \varphi)$ in Eq. (1)).

Two sampling tessellations provided by the SPHARM-MAT are exhibited in Fig. 1. In current study, the quadrangular tessellation with $65 \times 65 = 4225$ sampling points (sampling intervals $\Delta\theta = \pi/65 \approx 0.0483\,rad$, $\Delta\varphi = 2\pi/65 \approx 0.0967\,rad$) is adopted, as shown in Fig. 1(c). Further, the reconstructed SH-surface can be expressed by [33–36]

$$\begin{cases} x(\theta, \varphi) \approx \sum_{n=0}^{N} \sum_{m=-n}^{n} c_{xn}^m Y_n^m(\theta, \varphi) \\ y(\theta, \varphi) \approx \sum_{n=0}^{N} \sum_{m=-n}^{n} c_{yn}^m Y_n^m(\theta, \varphi) \\ z(\theta, \varphi) \approx \sum_{n=0}^{N} \sum_{m=-n}^{n} c_{zn}^m Y_n^m(\theta, \varphi) \end{cases}, \quad \theta \in [0, \pi], \ \varphi \in [0, 2\pi] \tag{1}$$

where the undermined coefficients c_{xn}^m, c_{yn}^m, and c_{zn}^m are estimated by the standard least squares method. While $Y_n^m(\theta, \phi)$ is the so-called SH function, and integers m and n are referred to as the degree and order of SH function, respectively. In this study, the integer N is set to be 15, which has been validated to be adequate for reconstruction of natural sand particles [35,36]. Any individual SH-surface has a unique set of coefficients. Note that the coefficients c_{xn}^m, c_{yn}^m, or c_{zn}^m will be complex number if the complex-valued SH function is adopted. It has been validated that the SH-surface reconstructed from the complex-valued and real-valued SHs with the same degree and order are identical [30,36].

For the real-valued SH function adopted in this study, it can be expressed as

$$Y_n^m(\theta, \varphi) = \begin{cases} \sqrt{\frac{(2n+1)(n-|m|)!}{4\pi(n+|m|)!}} P_n^{|m|}(\cos\theta) \sin(|m|\,\varphi), & m < 0 \\ \sqrt{\frac{(2n+1)(n-m)!}{4\pi(n+m)!}} P_n^m(\cos\theta) \cos(m\varphi), & m \geqslant 0 \end{cases} \tag{2}$$

where the associated Legendre function $P_n^m(\cos\theta)$ with degree n and order m is defined as

$$P_n^m(x) = (-1)^m (1 - x^2)^{m/2} \frac{d^m}{dx^m} P_n(x) \tag{3}$$

where $P_n(x)$ is the Legendre polynomial with degree n and can be given by

$$P_n(x) = \frac{1}{2^n n!} \frac{d^n}{dx^n} (x^2 - 1)^n \tag{4}$$

Meanwhile, Eq. (1) can deduce the center (x_c, y_c, z_c) of reconstructed SH-surface when $N = 0$, that reads

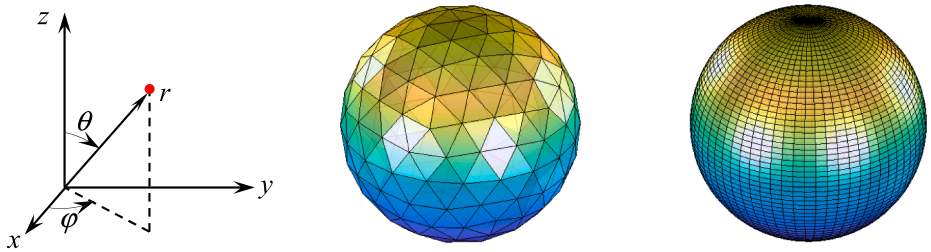

(a) Spherical coordinate system (b) Triangular tessellation (c) Quadrangular tessellation

Fig. 1. Spherical coordinate system and sampling tessellations.

$$\begin{cases} x_c = c_{x0}^0 Y_0^0 \\ y_c = c_{y0}^0 Y_0^0 \\ z_c = c_{y0}^0 Y_0^0 \end{cases} \tag{5}$$

where $Y_0^0 = \sqrt{1/\pi}/2$.

On the other hand, Eq. (1) can be rewritten in matrix form as

$$\boldsymbol{x} = \begin{bmatrix} x(\theta,\varphi) \\ y(\theta,\varphi) \\ z(\theta,\varphi) \end{bmatrix}_{3\times 1} = \begin{bmatrix} c_{x0}^0 & c_{x1}^{-1} & c_{x1}^0 & c_{x1}^1 & \cdots & c_{xN}^N \\ c_{y0}^0 & c_{y1}^{-1} & c_{y1}^0 & c_{y1}^1 & \cdots & c_{yN}^N \\ c_{z0}^0 & c_{z1}^{-1} & c_{z1}^0 & c_{z1}^1 & \cdots & c_{zN}^N \end{bmatrix}_{3\times(n+1)^2} \begin{bmatrix} Y_0^0(\theta,\varphi) \\ Y_1^{-1}(\theta,\varphi) \\ \vdots \\ Y_N^N(\theta,\varphi) \end{bmatrix}_{(n+1)^2\times 1} = \boldsymbol{C}_{\mathrm{SH}}\boldsymbol{Y} \tag{6}$$

where $\boldsymbol{C}_{\mathrm{SH}}$ is called the SH coefficient matrix, $\boldsymbol{Y}$ is referred to as the SH function vector. From the standpoint of geometry, the movement of any SH-body can be seen as the result of a series of coordinate transformations, including rotation, scaling, and translation transformations.

At time $t = t_k$ (the k-th time step), firstly, consider a rotation transformation of vector $\boldsymbol{x}^k = (x^k(\theta,\varphi), y^k(\theta,\varphi), z^k(\theta,\varphi))^{\mathrm{T}}$ around the center $\boldsymbol{x}_c^k = (x_c^k, y_c^k, z_c^k)^{\mathrm{T}}$ of SH-body, we have

$$^{\circ}\boldsymbol{x} = \boldsymbol{R}(\boldsymbol{x}^k - \boldsymbol{x}_c^k) + \boldsymbol{x}_c^k = \boldsymbol{R}\boldsymbol{C}_{\mathrm{SH}}^k\boldsymbol{Y} + (\boldsymbol{I} - \boldsymbol{R})\boldsymbol{x}_c^k \tag{7}$$

where $^{\circ}\boldsymbol{x} = (\,^{\circ}x(\theta,\varphi), {}^{\circ}y(\theta,\varphi), {}^{\circ}z(\theta,\varphi))^{\mathrm{T}}$ is the new Cartesian coordinate after the rotation transformation, and $\boldsymbol{I}$ is the 3×3 identity matrix. The 3×3 rotation matrix $\boldsymbol{R}$ is defined as

$$\boldsymbol{R} = \begin{bmatrix} \cos r_y \cos r_z & \sin r_x \sin r_y \cos r_z - \cos r_x \sin r_z & \cos r_x \sin r_y \cos r_z + \sin r_x \sin r_z \\ \cos r_y \sin r_z & \sin r_x \sin r_y \sin r_z + \cos r_x \cos r_z & \cos r_x \sin r_y \sin r_z - \sin r_x \cos r_z \\ -\sin r_y & \sin r_x \cos r_y & \cos r_x \cos r_y \end{bmatrix}, \tag{8}$$

where r_x, r_y, and r_z are the three Euler angles around x-, y-, and z-axis, respectively. Secondly, consider a scaling transformation of vector $^{\circ}\boldsymbol{x} = (^{\circ}x(\theta,\varphi), {}^{\circ}y(\theta,\varphi), {}^{\circ}z(\theta,\varphi))^{\mathrm{T}}$ with respect to the center $\boldsymbol{x}_c^k = (x_c^k, y_c^k, z_c^k)^{\mathrm{T}}$ of SH-body, reading

$$^{\cdot}\boldsymbol{x} = \boldsymbol{S}(^{\circ}\boldsymbol{x} - \boldsymbol{x}_c^k) + \boldsymbol{x}_c^k = \boldsymbol{S}\boldsymbol{R}\boldsymbol{C}_{\mathrm{SH}}^k\boldsymbol{Y} + (\boldsymbol{I} - \boldsymbol{S}\boldsymbol{R})\boldsymbol{x}_c^k \tag{9}$$

where $^{\cdot}\boldsymbol{x} = (\,^{\cdot}x(\theta,\varphi), \,^{\cdot}y(\theta,\varphi), \,^{\cdot}z(\theta,\varphi))^{\mathrm{T}}$ is the new Cartesian coordinate after the rotation and scaling transformation, and the 3×3 scaling matrix $\boldsymbol{S}$ is given by

$$\boldsymbol{S} = \begin{bmatrix} S_x & 0 & 0 \\ 0 & S_y & 0 \\ 0 & 0 & S_z \end{bmatrix} \tag{10}$$

where S_x, S_y, and S_z are the scaling factors along x-, y-, and z-axis, respectively. It is worth mention that scaling operation is needed to enlarge or reduce the particle size during preparation process of a packing.

Finally, adding a translational increment $\bar{\boldsymbol{x}}$ to Eq. (9) yields the updated coordinates at t_{k+1}:

$$\boldsymbol{x}^{k+1} = {}^{\cdot}\boldsymbol{x} + \bar{\boldsymbol{x}} \tag{11}$$

Eq. (11) can be recast as

$$\boldsymbol{x}^{k+1} = \boldsymbol{C}_{\mathrm{SH}}^{k+1}\boldsymbol{Y} + \Delta\boldsymbol{x}^k \tag{12}$$

where

$$\boldsymbol{C}_{\mathrm{SH}}^{k+1} = \boldsymbol{S}\boldsymbol{R}\boldsymbol{C}_{\mathrm{SH}}^k \tag{13}$$

$$\Delta\boldsymbol{x}^k = (\boldsymbol{I} - \boldsymbol{S}\boldsymbol{R})\boldsymbol{x}_c^k + \bar{\boldsymbol{x}} \tag{14}$$

Such that the center $\boldsymbol{x}_c^{k+1} = (x_c^{k+1}, y_c^{k+1}, z_c^{k+1})^{\mathrm{T}}$ of reconstructed SH-surface can be updated as

$$\boldsymbol{x}_c^{k+1} = \boldsymbol{x}_c^k + \bar{\boldsymbol{x}} \tag{15}$$

Note that Eq. (13) suggests that the SH coefficient matrix $\boldsymbol{C}_{\mathrm{SH}}^{k+1}$ at t_{k+1} can be obtained recursively from $\boldsymbol{C}_{\mathrm{SH}}^k$ at the previous step. Once $\boldsymbol{C}_{\mathrm{SH}}$ is calculated by Eq. (6) for $t = 0$, the subsequent SH coefficient matrix can be simply updated by rotation and scaling operations via Eq. (13) at each step, resulting in a highly efficient algorithm. Eq. (12) gives us a new SH-surface after rotation, scaling, and translation transformations. The SH-surface forms the basis of the geometric iteration algorithm for contact detection, as shown in Section 4 for details.

3. Dynamics of SH-body

In this section, we assume firstly the SH-body is perfect rigid. Then the motion of SH-body will be formulated within the framework of DDA. Therefore, the treatments on inertia, external load, and displacement constraints are the same as the original DDA [37]. Meanwhile, the Newmark time integration scheme is still adopted to discretize temporal domain. Thus, the resulted method inherits the unconditional stability of the original DDA.

3.1. Equations of motion

Fig. 2 shows a rigid SH-body under loading and constrains. Point C is the center of the SH-body, and $\boldsymbol{F}$, $\boldsymbol{G}$, and $\bar{\boldsymbol{p}}$ are the point loading, the gravity, and the distributed loading, respectively. Moreover, $\bar{\boldsymbol{u}}$ is the specified displacement constraints. Following the original DDA [37] and using the Newmark time integration scheme (algorithm parameters $\gamma = 1.0$ and $\beta = 0.5$), we can obtain the equation of motion for rigid SH-body-i

$$\frac{2}{\Delta t^2}\boldsymbol{M}_i\Delta\boldsymbol{d}_i = \boldsymbol{f}_i \tag{16}$$

where $\boldsymbol{M}_i$ and $\boldsymbol{f}_i$ are the 6×6 equivalent mass matrix and the 6×1 equivalent force vector, respectively, and Δt is the time step. Note that the initial velocity is contained in $\boldsymbol{f}_i$. The increment of DOF is given by

$$\Delta\boldsymbol{d}_i = [\Delta u_c, \ \Delta v_c, \ \Delta w_c, \ \Delta r_x, \ \Delta r_y, \ \Delta r_z]^{\mathrm{T}} \tag{17}$$

where Δu_c, Δv_c, and Δw_c are three translational increments of the centroid of the body, Δr_x, Δr_y, and Δr_z are three rotation angle increments of the rigid-body.

After solving Eq. (16), to eliminate the nonphysical expansion of a rigid body existing in the original DDA, the increments of displacement at any point within the SH-body is obtained from

$$\begin{bmatrix} \Delta u \\ \Delta v \\ \Delta w \end{bmatrix} = \underbrace{\begin{bmatrix} \Delta u_c \\ \Delta v_c \\ \Delta w_c \end{bmatrix}}_{\text{Translation components}} + \underbrace{(\boldsymbol{R} - \boldsymbol{I})\begin{bmatrix} x - x_c \\ y - y_c \\ z - z_c \end{bmatrix}}_{\text{Rotation components}} \tag{18}$$

where $\boldsymbol{I}$ is identity matrix, $\boldsymbol{R}$ is a rotation matrix defined in Eq. (9) and is calculated by replacing r_x, r_y, and r_z with Δr_x, Δr_y, and Δr_z, respectively.

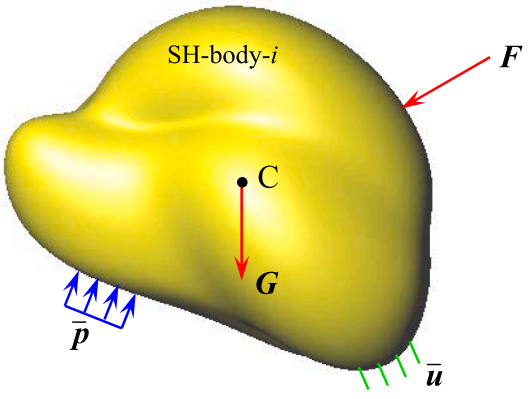

Fig. 2. Constraints and loading on a rigid SH-body.

Eq. (18) is the so-called the rotation martix modification method [52], which allows a rigid body to undergo any arbitrary large rotation without the change in both volume and shape. In Eq. (16), the equivalent mass matrix and equivalent force vector involve volume integrals that can be boiled down to the following ten formulas: $S = \iiint dV$, $S_x = \iiint x dV$, $S_y = \iiint y dV$, $S_z = \iiint z dV$, $S_{xx} = \iiint x^2 dV$, $S_{yy} = \iiint y^2 dV$, $S_{zz} = \iiint z^2 dV$, $S_{yz} = \iiint yz dV$, $S_{zx} = \iiint zx dV$, and $S_{xy} = \iiint xy dV$. Mathematically, although the variables x, y, and z can be expressed explicitly as a analytic function of the two angle parameters θ and φ (refer to Eq. (1)), they all have a large number of terms, which makes that the above ten formulas too complex to be calculated analytically with ease. Thus, in this study, we still adopt the simplex integration method [53] to compute the relevant volume integrals based on discrete vertexes.

Note that $S = \iiint dV$ is just the volume of SH-body, thus, it is a constant. Next, we will deduce the recursion formula for calculating the other nine volume integrals from time step k to time step $k + 1$. Based on Eq. (18), we have

$$\mathbf{x}^{k+1} = \mathbf{R}\,\mathbf{x}^{k} + (\mathbf{I} - \mathbf{R})\mathbf{x}_{\mathrm{c}}^{k} + \Delta\mathbf{u}_{\mathrm{c}} \tag{19}$$

where $\Delta\boldsymbol{u}_{\mathrm{c}} = [\Delta u_{\mathrm{c}}, \Delta v_{\mathrm{c}}, \Delta w_{\mathrm{c}}]^{\mathrm{T}}$. Then, the three integrals S_x, S_y, and S_z can be computed from

$$\begin{aligned}[S_x^{k+1},\ S_y^{k+1},\ S_z^{k+1}]^{\mathrm{T}} &= \int \mathbf{x}^{k+1} dV \\ &= \int \mathbf{R}x^{k} dV + \int (\mathbf{I} - \mathbf{R})\mathbf{x}_{\mathrm{c}}^{k} dV + \int \Delta\mathbf{u} dV\end{aligned} \tag{20}$$

Further, we have

$$[S_x^{k+1},\ S_y^{k+1},\ S_z^{k+1}]^{\mathrm{T}} = \boldsymbol{R}[S_x^{k},\ S_y^{k},\ S_z^{k}]^{\mathrm{T}} + S[(\boldsymbol{I} - \boldsymbol{R})\boldsymbol{x}_{\mathrm{c}}^{k} + \Delta\boldsymbol{u}] \tag{21}$$

As for the last six integrals, from Eq. (19), one can construct an interim matrix, reading

$$\begin{aligned}\begin{bmatrix} S_{xx}^{k+1} & S_{xy}^{k+1} & S_{xz}^{k+1} \\ S_{yx}^{k+1} & S_{yy}^{k+1} & S_{yz}^{k+1} \\ S_{zx}^{k+1} & S_{zy}^{k+1} & S_{zz}^{k+1} \end{bmatrix} &= \int \mathbf{x}^{k+1}(\mathbf{x}^{k+1})^{\mathrm{T}} dV \\ &= \int \mathbf{R}\mathbf{x}^{k}(\mathbf{R}\mathbf{x}^{k})^{\mathrm{T}} dV + \int (\mathbf{I} - \mathbf{R})\mathbf{x}_{\mathrm{c}}^{k}[(\mathbf{I} - \mathbf{R})\mathbf{x}_{\mathrm{c}}^{k}]^{\mathrm{T}} dV + \int \Delta\mathbf{u}(\Delta\mathbf{u})^{\mathrm{T}} dV\end{aligned} \tag{22}$$

After some mathematical manipulations, we can obtain

$$\begin{bmatrix} S_{xx}^{k+1} & S_{xy}^{k+1} & S_{xz}^{k+1} \\ S_{yx}^{k+1} & S_{yy}^{k+1} & S_{yz}^{k+1} \\ S_{zx}^{k+1} & S_{zy}^{k+1} & S_{zz}^{k+1} \end{bmatrix} = \boldsymbol{R}\begin{bmatrix} S_{xx}^{k} & S_{xy}^{k} & S_{xz}^{k} \\ S_{yx}^{k} & S_{yy}^{k} & S_{yz}^{k} \\ S_{zx}^{k} & S_{zy}^{k} & S_{zz}^{k} \end{bmatrix}\boldsymbol{R}^{\mathrm{T}} + S\{(\boldsymbol{I} - \boldsymbol{R})\boldsymbol{x}_{\mathrm{c}}^{k}[(\boldsymbol{I} - \boldsymbol{R})\boldsymbol{x}_{\mathrm{c}}^{k}]^{\mathrm{T}} + \Delta\boldsymbol{u}(\Delta\boldsymbol{u})^{\mathrm{T}}\} \tag{23}$$

The elements in the upper triangular matrix of the interim matrix are the desired last six integrals. Eqs. (20) and (23) imply that the simplex integrations are needed to be calculated only at the initial time step (i.e. $t = 0$). For the subsequent time steps, the abovementioned ten volume integrals can be obtained recursively according to Eqs. (20) and (23). In this way, the computational cost can be reduced significantly.

3.2. Treatment of contact

In this section, we will extend the variational or quasi-variational inequality formulation dealing with contact for the two-dimensional settings [50] to the three-dimensional cases. Firstly, we will define the contact points and the directions of contact force, as shown in Fig. 3.

Consider a scenario where two SH-bodies, SH-body-i and SH-body-j (assume $i < j$), draw close to each other, points A and B are the closest points between them (refer to Section 4 for more details). In this study, line AB is called as the normal contact line. If the length of line AB is less than a preset tolerance d_{contact}, then a pair of contact has been detected. The mid-point of line AB is divided into two contact points C_1 and C_2, which belong to SH-body-i and SH-body-j, respectively. As our convention, the unit contact normal vector $\boldsymbol{n}$ is parallel to line AB and points to the interior of the SH-body with a smaller global index, namely, SH-body-i ($i < j$), as presented in Fig. 3. At the beginning of the current time step, points C_1 and C_2 are superimposed. Without regard to the contact force, assume that points C_1 and C_2 move to point C_1^* and C_2^* at the end of the current time step, respectively. From point C_2^* to point C_1^* we have a relative displacement vector $\boldsymbol{g} = \overrightarrow{C_2^* C_1^*} = C_1^* - C_2^*$, which can be expressed as $\boldsymbol{g} = g^n\boldsymbol{n} + g^\tau\boldsymbol{\tau}$. Thus, the unit contact tangent vector can be obtained from $\boldsymbol{\tau} = (\boldsymbol{g} - g^n\boldsymbol{n})/|\boldsymbol{g} - g^n\boldsymbol{n}|$.

Some loadings and constraints on a rigid SH-body have been considered in the previous section. Now, let us pay attention to the contact forces $\boldsymbol{p}_1$, $\boldsymbol{p}_2$, …, $\boldsymbol{p}_k$, and $\boldsymbol{p}_m$ (m is assumed to be the total number of contact-pairs) on the rigid SH-body-i, as illustrated in Fig. 4. For any contact force $\boldsymbol{p}_k$, we have $\boldsymbol{p}_k = p_k^n\boldsymbol{n} + p_k^\tau\boldsymbol{\tau}$. Note that the vectors $\boldsymbol{n}$ and $\boldsymbol{\tau}$ are not necessarily parallel to the global coordinate system. To introduce these contact forces into Eq. (16) with respect to the global coordinate system, we should need the transform matrix

$$\boldsymbol{C}_i = [\boldsymbol{C}_i^1, \boldsymbol{C}_i^2, \cdots, \boldsymbol{C}_i^k, \cdots, \boldsymbol{C}_i^{m_i}] \tag{24}$$

where m_i is assumed to be the total number of these contact forces on the SH-body-i. And each $\boldsymbol{C}_i^{\,k}$ is the 6 × 2 matrix associated with the k-th contact-pair on the SH-body-i, reading

$$\boldsymbol{C}_i^{\,k}(x_k, y_k, z_k) = s_k\boldsymbol{T}_i^{\,\mathrm{T}}(x_k, y_k, z_k)[\boldsymbol{n}_k, \boldsymbol{\tau}_k], \quad k = 1, \cdots, m_i \tag{25}$$

where (x_k, y_k, z_k) are the coordinates of the k-th contact point at the beginning of the current time step. Note that s_k is a sign function to consider the definition of unit vectors $\boldsymbol{n}_k$ and $\boldsymbol{\tau}_k$. Note that the contact forces always come in pairs. Complying with the definitions of the unit vectors $\boldsymbol{n}_k$ and $\boldsymbol{\tau}_k$ (refer to Fig. 3) of the k-th contact-pair, if $i < j$, s_k associated with SH-body-i is a positive sign (+), while s_k related to SH-body-j is a negative sign (−). Additionally, the 3 × 2 matrix $[\boldsymbol{n}_k, \boldsymbol{\tau}_k]$ is defined as

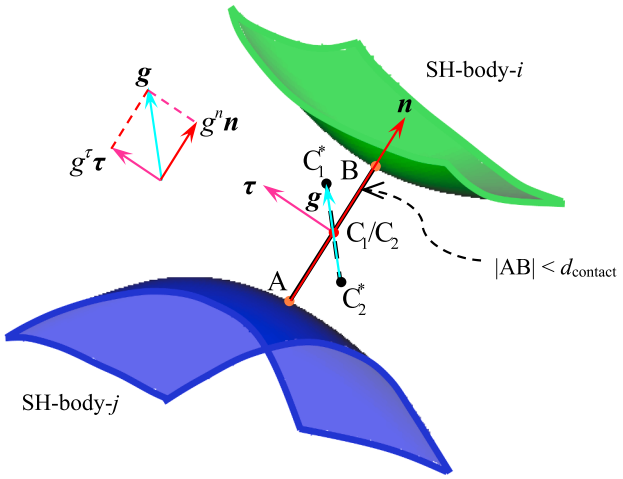

Fig. 3. Contact points and contact directions ($i < j$).

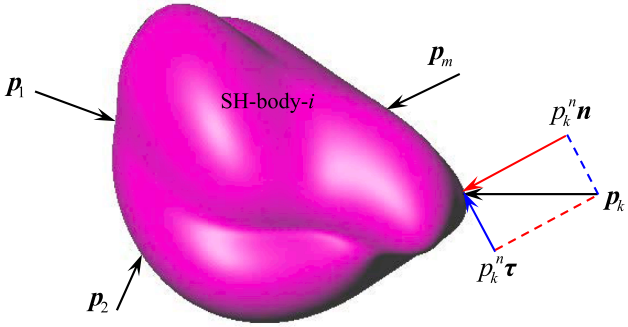

Fig. 4. Contact force on a rigid SH-body.

$$[\boldsymbol{n}_k,\ \boldsymbol{\tau}_k] = \begin{bmatrix} \cos\alpha_k{}^n & \cos\alpha_k{}^\tau \\ \cos\beta_k{}^n & \cos\beta_k{}^\tau \\ \cos\gamma_k{}^n & \cos\gamma_k{}^\tau \end{bmatrix} \tag{26}$$

where $(\cos\alpha_k{}^n,\ \cos\beta_k{}^n,\ \cos\gamma_k{}^n)$ and $(\cos\alpha_k{}^\tau,\ \cos\beta_k{}^\tau,\ \cos\gamma_k{}^\tau)$ are the direction cosines of the vectors $\boldsymbol{n}_k$ and $\boldsymbol{\tau}_k$, respectively. For these n_i contact forces on SH-body-i, we can further construct a non-negative contact vector $\boldsymbol{p}_i$

$$\boldsymbol{p}_i = [p_1^n,\ p_1^\tau,\ p_2^n,\ p_2^\tau, \cdots, p_{mi}^n,\ p_{mi}^\tau]^{\mathrm{T}} \tag{27}$$

Finally, by introducing the contact forces the governing equation Eq. (16) becomes

$$\frac{2}{\Delta t^2}\boldsymbol{M}_i\Delta\boldsymbol{d}_i - \boldsymbol{C}_i\boldsymbol{p}_i = \boldsymbol{f}_i \tag{28}$$

In fact, Eq. (28) (considering the contact forces) can be interpreted as a "correction" of Eq. (16) (without considering the contact forces). Therefore, the total of increment of DOF can be rewritten as the superposition of two components, reading

$$\Delta\boldsymbol{d}_i = \Delta\boldsymbol{d}_i^p + \Delta\,\boldsymbol{d}_i^f \tag{29}$$

where $\Delta\boldsymbol{d}_i^p$ and $\Delta\boldsymbol{d}_i^f$ are the contributions of the contact force vector $\boldsymbol{p}_i$ and the equivalent force vector $\boldsymbol{f}_i$, respectively. And

$$\begin{aligned} \Delta\boldsymbol{d}_i^f &= \tfrac{\Delta t^2}{2}\boldsymbol{M}_i^{-1}\boldsymbol{f}_i \\ \Delta\boldsymbol{d}_i^p &= \tfrac{\Delta t^2}{2}\boldsymbol{M}_i^{-1}\boldsymbol{C}_i\boldsymbol{p}_i \end{aligned} \tag{30}$$

On the other hand, from Fig. 3 we have known that we can construct a relative displacement vector $\boldsymbol{R}_k = \overrightarrow{C_2^*C_1^*} = C_1^* - C_2^*$ for the k-th contact-pair without considering the contact forces. Assume that (x_i, y_i, z_i) and (x_j, y_j, z_j) are the coordinates of the contact point C_1^* and C_2^*, respectively. Then, the normal component of $g_k{}^n$ can be given by

$$g_k^n = \boldsymbol{n}_k^{\mathrm{T}}\cdot(\boldsymbol{x}_i - \boldsymbol{x}_j) \tag{31}$$

where

$$\begin{aligned} \mathbf{x}_l &= [x_l, y_l, z_l]^{\mathrm{T}} \\ &= [x_l{}^0, y_l{}^0, z_l{}^0]^{\mathrm{T}} + \mathbf{T}(x_l{}^0, y_l{}^0, z_l{}^0)(\Delta\mathbf{d}_l^f + \Delta\mathbf{d}_l^p), \quad l = i, j \end{aligned} \tag{32}$$

and superscript "0" denotes the initial coordinates of contact points,

$$\boldsymbol{T}(x, y, z) = \begin{bmatrix} 1 & 0 & 0 & 0 & z - z_c & y_c - y \\ 0 & 1 & 0 & z_c - z & 0 & x - x_c \\ 0 & 0 & 1 & y - y_c & x_c - x & 0 \end{bmatrix} \tag{33}$$

where (x_c, y_c, z_c) is the coordinate of the center of the SH-body-l. Likely, the tangent component of $\boldsymbol{g}_k$ can be defined as

$$g_k^\tau = \boldsymbol{\tau}_k^{\mathrm{T}}\cdot(\boldsymbol{x}_i - \boldsymbol{x}_j) \tag{34}$$

In the current study, the components $g_k{}^n$ and $g_k{}^\tau$ are also referred to as the normal contact gap and the tangent contact gap, respectively. If necessary, we can adopt the Coulomb friction law $\tau(p_k{}^n) = c_k + \mu_k p_k{}^n$

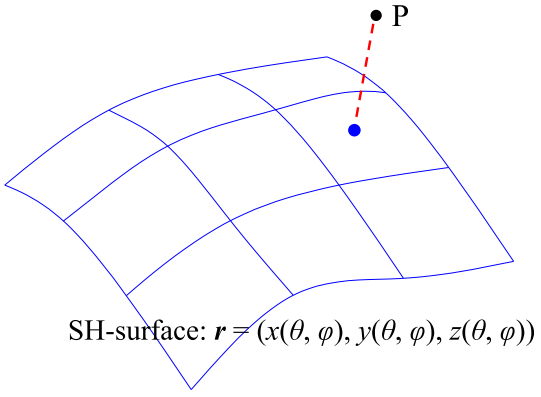

Fig. 5. Closest point between point P and SH-surface.

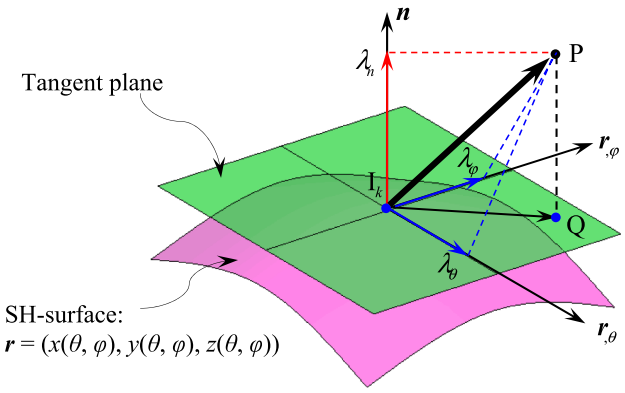

Fig. 6. First order geometric iteration method.

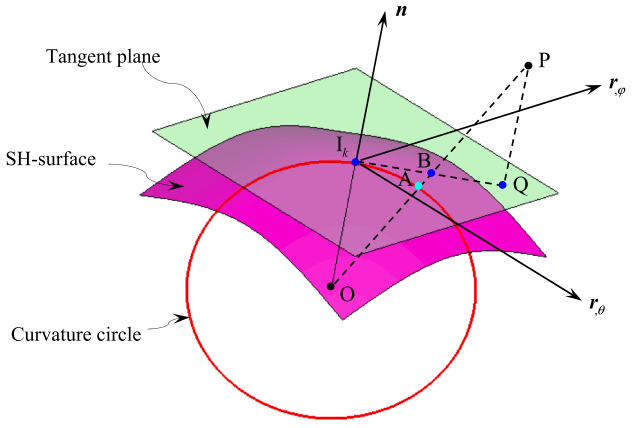

Fig. 7. Second-order geometric iteration method.

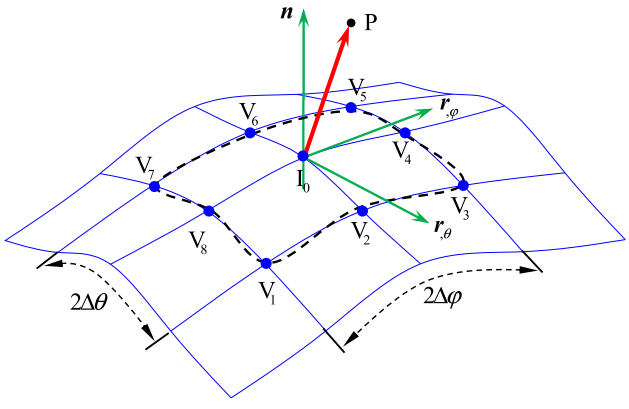

Fig. 8. Iteration search zone.

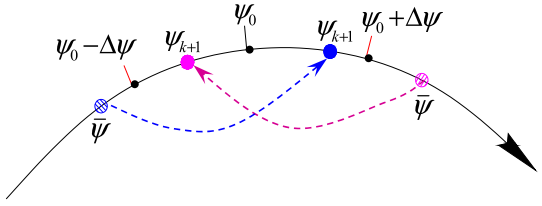

Fig. 9. Limitation of angles ($\psi = \theta,\ \varphi$).

(here, c_k is the cohesion of the contact surface, μ_k is the sliding friction coefficient) to take into account the friction-induced shear contact force ${p_k}^{\tau}$, which should fall in the interval of $[-\tau({p_k}^{n}), \tau({p_k}^{n})]$. Meanwhile, ${g_k}^{n}$ and ${g_k}^{\tau}$ are both the function in terms of ${p_k}^{\tau}$ and ${p_k}^{n}$. Assume that there are N contact-pairs in total system at the current time step, by applying the theory of finite-dimensional variational inequality, we have the equivalent variational or quasi-variational inequality format for the contact force: find the global contact force vector $\boldsymbol{p} \in X(\boldsymbol{p}) \subset R^{2N}$, such that

$$(\boldsymbol{q}-\boldsymbol{p})^{\mathrm{T}}\boldsymbol{G}(\boldsymbol{p}) \geqslant 0, \quad \forall\, \boldsymbol{q} \in X(\boldsymbol{p}) \tag{35}$$

where the contact gap function $\boldsymbol{G}(\boldsymbol{p})$ is given by

$$\boldsymbol{G}(\boldsymbol{p}) = [{g_1}^{n}(\boldsymbol{p}), {g_1}^{\tau}(\boldsymbol{p}), \cdots, {g_N}^{n}(\boldsymbol{p}), {g_N}^{\tau}(\boldsymbol{p})]^{\mathrm{T}} \tag{36}$$

and the global contact force vector is

$$\boldsymbol{p} = [{p_1}^{n}, {p_1}^{\tau}, \cdots, {p_N}^{n}, {p_N}^{\tau}]^{\mathrm{T}} \tag{37}$$

The constraint $X(\boldsymbol{p})$ is a closed set in R^{2N}, which dependents on the global contact force vector $\boldsymbol{p}$, and is defined as

$$X(\boldsymbol{p}) = X_1({p_1}^{n}) \times X_2({p_2}^{n}) \times \cdots \times X_N({p_N}^{n}) \tag{38}$$

where $X_k({p_k}^{n}) \subset R^2$ is the constraint set of the contact forces ${p_k}^{n}$ and ${p_k}^{\tau}$ in the k-th contact pair, which dependents on the normal contact force ${p_k}^{n}$ of the k-th contact-pair and is expressed as

$$X_k({p_k}^{n}) = \{({q_k}^{n}, {q_k}^{\tau}) | {q_k}^{n} \geqslant 0, |{q_k}^{\tau}| \leqslant \tau({p_k}^{n})\} = [0, \infty) \times [-\tau({p_k}^{n}), \tau({p_k}^{n})] \tag{39}$$

Then, the compatibility iteration [50] based on the projection-contraction algorithm [54] can be utilized to solve the contact forces. One can refer to Refs. [50] and [54] for more details. As thus, we can bypass the use of artificial contact spring, whose value is usually problem dependent and is difficult to determine. Moreover, we can also avoid the open-close iteration, whose convergence has not yet been proven.

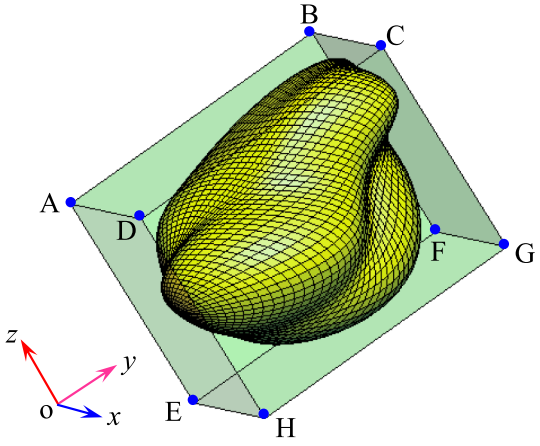

Fig. 10. A SH-body and its external box ABCDEFGH.

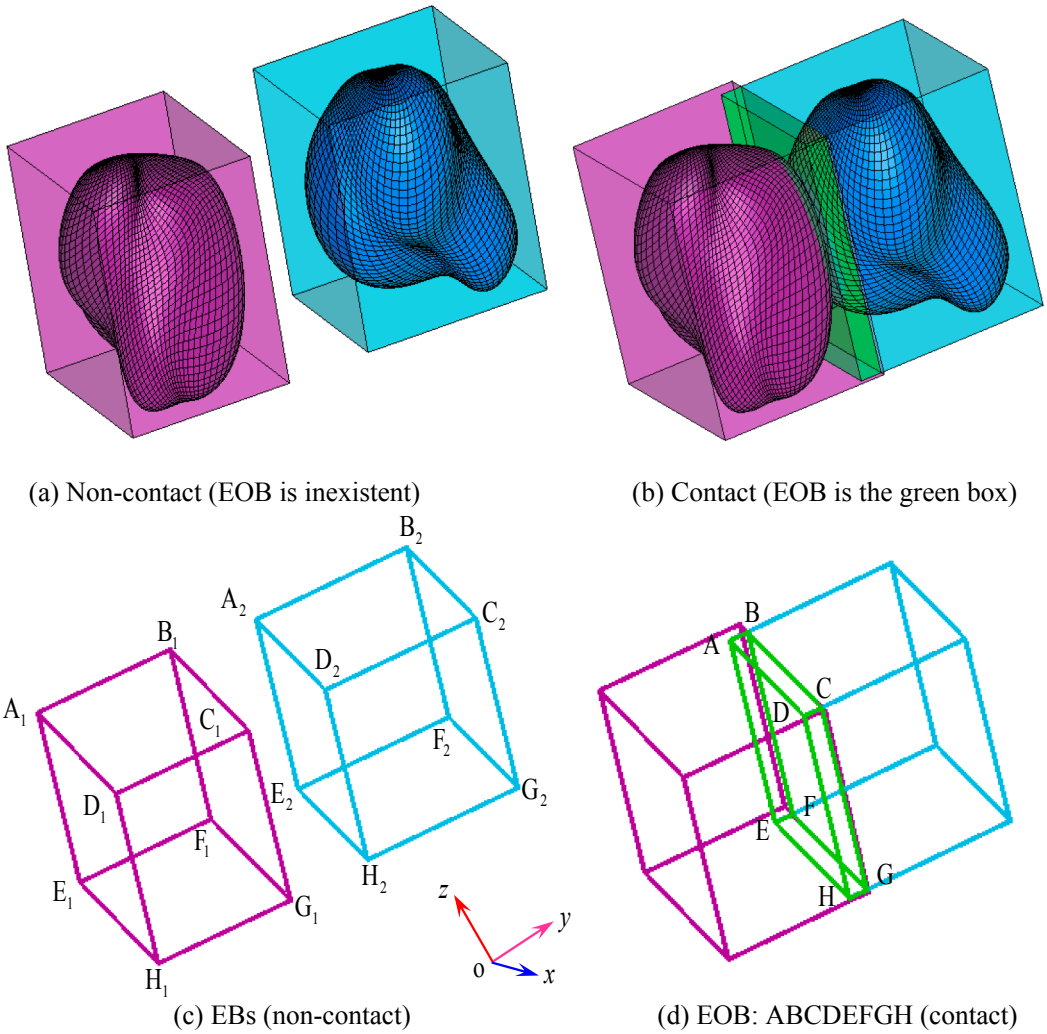

Fig. 11. Two SH-bodies and their external overlapping box (EOB).

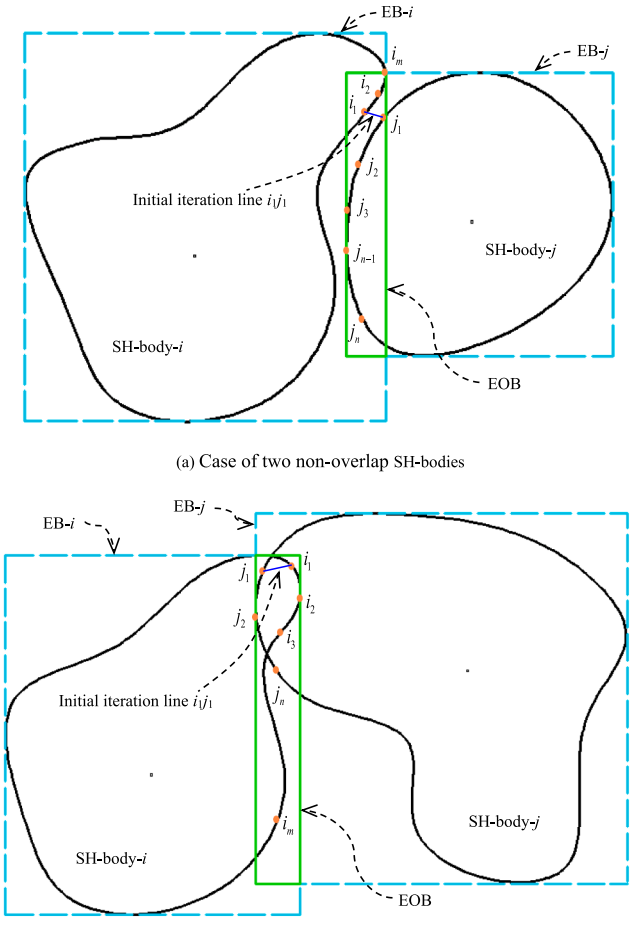

Fig. 12. Two cases if there is an EOB between two SH-bodies.

4. Contact between two SH-bodies

By means of SH reconstruction, the particle surface (SH-surface) can described by three analytic functions, i.e. S: $\boldsymbol{r}(\theta, \varphi) = (x(\theta, \varphi), y(\theta, \varphi), z(\theta, \varphi))$, which is continuous and smooth.

4.1. The closest point between point and SH-surface

Consider point P that is outside of SH-surface S: $\boldsymbol{r}(\theta, \varphi) = (x(\theta, \varphi), y(\theta, \varphi), z(\theta, \varphi))$, as depicted in Fig. 5. We can construct the squared distance function between point P and SH-surface S

$$d = (x - x_P)^2 + (y - y_P)^2 + (z - z_P)^2 \tag{40}$$

where (x, y, z) represents a point on SH surface, while (x_P, y_P, z_P) are the Cartesian coordinates of point P. The substitution of Eq. (1) into Eq. (40) yields

$$\begin{aligned} d = &\left(\sum_{n=0}^{N} \sum_{m=-n}^{n} c_{xn}^{m} Y_n^m(\theta, \varphi) - x_P\right)^2 \\ &+ \left(\sum_{n=0}^{N} \sum_{m=-n}^{n} c_{yn}^{m} Y_n^m(\theta, \varphi) - y_P\right)^2 \\ &+ \left(\sum_{n=0}^{N} \sum_{m=-n}^{n} c_{zn}^{m} Y_n^m(\theta, \varphi) - z_P\right)^2 \end{aligned} \tag{41}$$

The closest point between point P and SH-surface S requires the following stationary conditions:

$$\frac{\partial d(\theta, \varphi)}{\partial \theta} = 0, \quad \frac{\partial d(\theta, \varphi)}{\partial \varphi} = 0 \tag{42}$$

which can be solved by using Newton-Raphson iteration method. Nevertheless, this method is known to be sensitive to initial iteration values and would be suffered numerical instability to failure. In this study, we mainly focus on the geometric iteration method to determine the closest point.

For a continuous and smooth surface, the closest point between it and a given point is the orthogonal projection of the point onto the surface. Next, we will extend the first-order geometric iteration method [48] and the second-order geometric iteration method [49] to SH-surface.

Assume that point I_k is the current iteration point and that k is the current iteration step. From point I_k to point P we can construct a vector $\overrightarrow{I_kP}$ that can be decomposed along tangent directions $\partial \boldsymbol{r}/\partial\theta$ and $\partial \boldsymbol{r}/\partial\varphi$, and unit external normal direction $\boldsymbol{n}$, respectively, as exhibited in Fig. 6. It is

$$\overrightarrow{I_kP} = \lambda_\theta \frac{\partial \boldsymbol{r}}{\partial \theta} + \lambda_\varphi \frac{\partial \boldsymbol{r}}{\partial \varphi} + \lambda_n \boldsymbol{n} \tag{43}$$

where λ_θ, λ_φ, and λ_n are the three components along the three

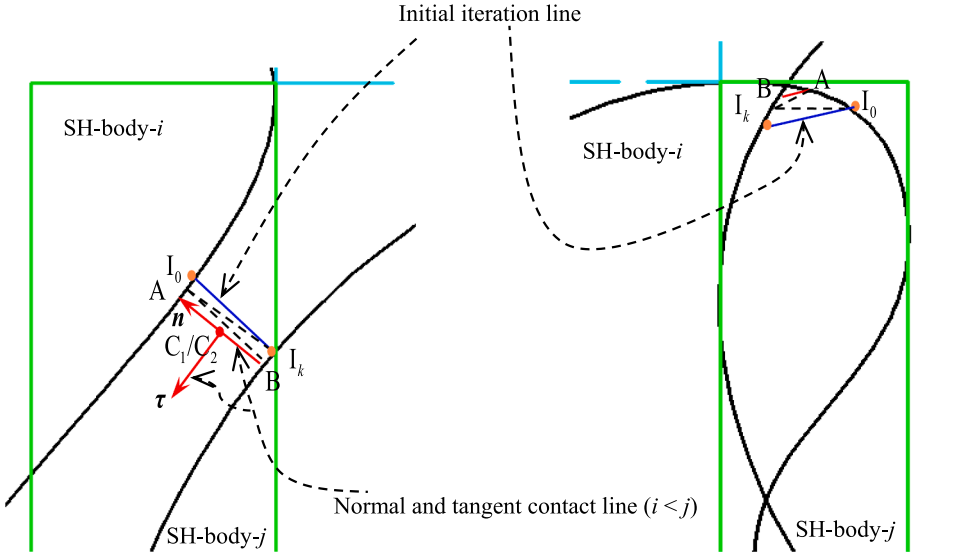

Fig. 13. Overlap checking of two cases.

directions, respectively. And

$$\begin{cases} \dfrac{\partial \boldsymbol{r}}{\partial \theta} = \boldsymbol{r}_{,\theta} = \left\{\dfrac{\partial x}{\partial \theta}, \dfrac{\partial y}{\partial \theta}, \dfrac{\partial z}{\partial \theta}\right\} \\ \dfrac{\partial \boldsymbol{r}}{\partial \varphi} = \boldsymbol{r}_{,\varphi} = \left\{\dfrac{\partial x}{\partial \varphi}, \dfrac{\partial y}{\partial \varphi}, \dfrac{\partial z}{\partial \varphi}\right\} \\ \boldsymbol{n} = \dfrac{\boldsymbol{r}_{,\theta} \times \boldsymbol{r}_{,\varphi}}{|\boldsymbol{r}_{,\theta} \times \boldsymbol{r}_{,\varphi}|} \end{cases} \tag{44}$$

By dot multiplying Eq. (43) with $\boldsymbol{r}_{,\theta}$ and $\boldsymbol{r}_{,\varphi}$, respectively, we can get

$$\begin{cases} \boldsymbol{r}_{,\theta} \cdot \overrightarrow{\mathrm{I}_k \mathrm{P}} = \lambda_\theta \boldsymbol{r}_{,\theta}^2 + \lambda_\varphi \boldsymbol{r}_{,\varphi} \cdot \boldsymbol{r}_{,\theta} \\ \boldsymbol{r}_{,\varphi} \cdot \overrightarrow{\mathrm{I}_k \mathrm{P}} = \lambda_\theta \boldsymbol{r}_{,\theta} \cdot \boldsymbol{r}_{,\varphi} + \lambda_\varphi \boldsymbol{r}_{,\varphi}^2 \end{cases} \tag{45}$$

so λ_θ and λ_φ can be calculated as the solution of a regular system of linear equations. Then, θ and φ can be updated by adding λ_θ and λ_φ, respectively [55], namely iteration increments $\delta\theta = \lambda_\theta$ and $\delta\varphi = \lambda_\varphi$. Note that the convergence of iteration will make vector $\overrightarrow{\mathrm{I}_k \mathrm{P}}$ and normal vector $\boldsymbol{n}$ are collinear. This implies $\delta\theta \to 0$ and $\delta\varphi \to 0$. Thus, there are two approaches to terminate the iteration. (1) The angle between $\overrightarrow{\mathrm{I}_k \mathrm{P}}$ and normal vector $\boldsymbol{n}$ is less than a pre-set angle tolerance, which is called the angle control approach in current paper. (2) $\delta\theta$ and $\delta\varphi$ are both less than a pre-given increment tolerance, which is referred as to the increment control approach in this study. The predetermined angle and increment tolerances depend on the requirement for accuracy.

The second-order geometric iteration method [49], which makes use of the second-order derivative of a surface, as described in Fig. 7. First, we have a direction as follows

$$\boldsymbol{c}_k' = \lambda_\theta \boldsymbol{r}_{,\theta} + \lambda_\varphi \boldsymbol{r}_{,\varphi} \tag{46}$$

Correspondingly, the normal curvature can be obtained from

$$k_n = [L\lambda_\theta^2 + 2M\lambda_\theta\lambda_\varphi + N\lambda_\varphi^2][E\lambda_\theta^2 + 2F\lambda_\theta\lambda_\varphi + G\lambda_\varphi^2]^{-1} \tag{47}$$

where E, F, and G are the coefficients of the first fundamental form of the surface, while L, M, and N are the coefficients of the second fundamental form of the same surface. They are defined as

$$\begin{aligned} &E = \boldsymbol{r}_{,\theta}^2, \quad F = \boldsymbol{r}_{,\theta} \cdot \boldsymbol{r}_{,\varphi}, \quad G = \boldsymbol{r}_{,\varphi}^2 \\ &L = \boldsymbol{r}_{,\theta\theta} \cdot \boldsymbol{n}, \quad M = \boldsymbol{r}_{,\theta\varphi} \cdot \boldsymbol{n}, \quad N = \boldsymbol{r}_{,\varphi\varphi} \cdot \boldsymbol{n} \end{aligned} \tag{48}$$

The corresponding curvature circle O has radius $1/k_n$ and center $\mathrm{I}_k + |\boldsymbol{n}/k_n$. Then, point A, which is the intersection point between line OP

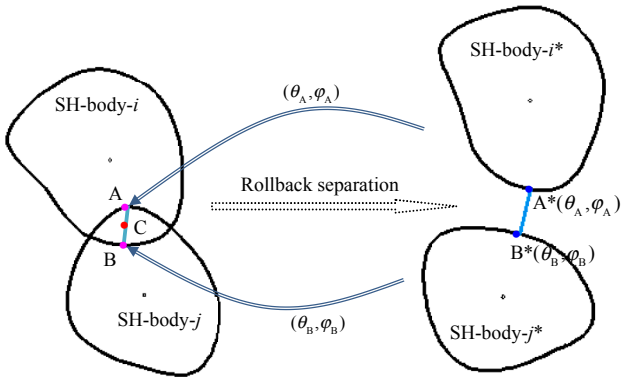

Fig. 15. "Separation-based" scheme for the case of two overlap SH-bodies.

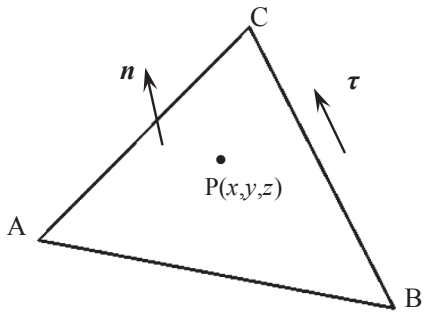

Fig. 16. Point on plane ABC.

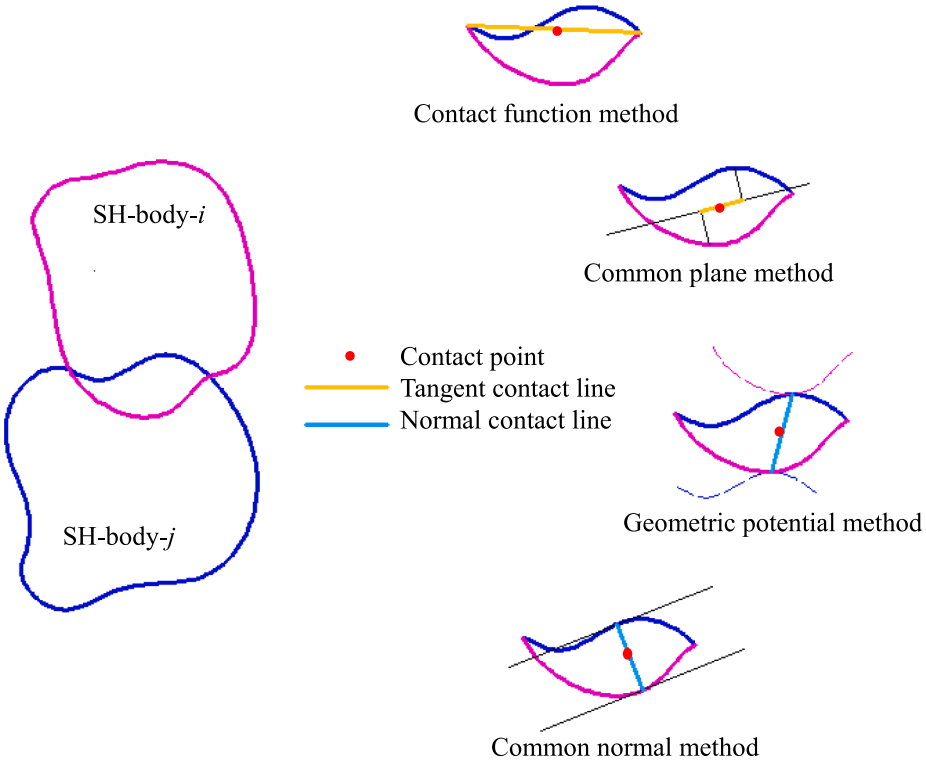

Fig. 14. "Overlap-based" scheme for two overlap SH-bodies.

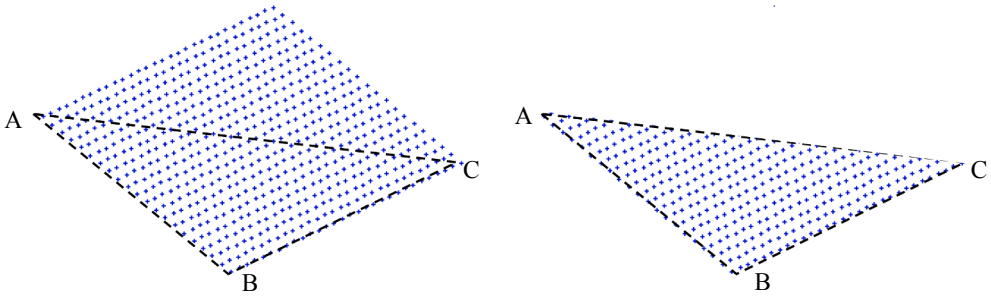

Fig. 17. Points distributing uniformly on plane ABC.

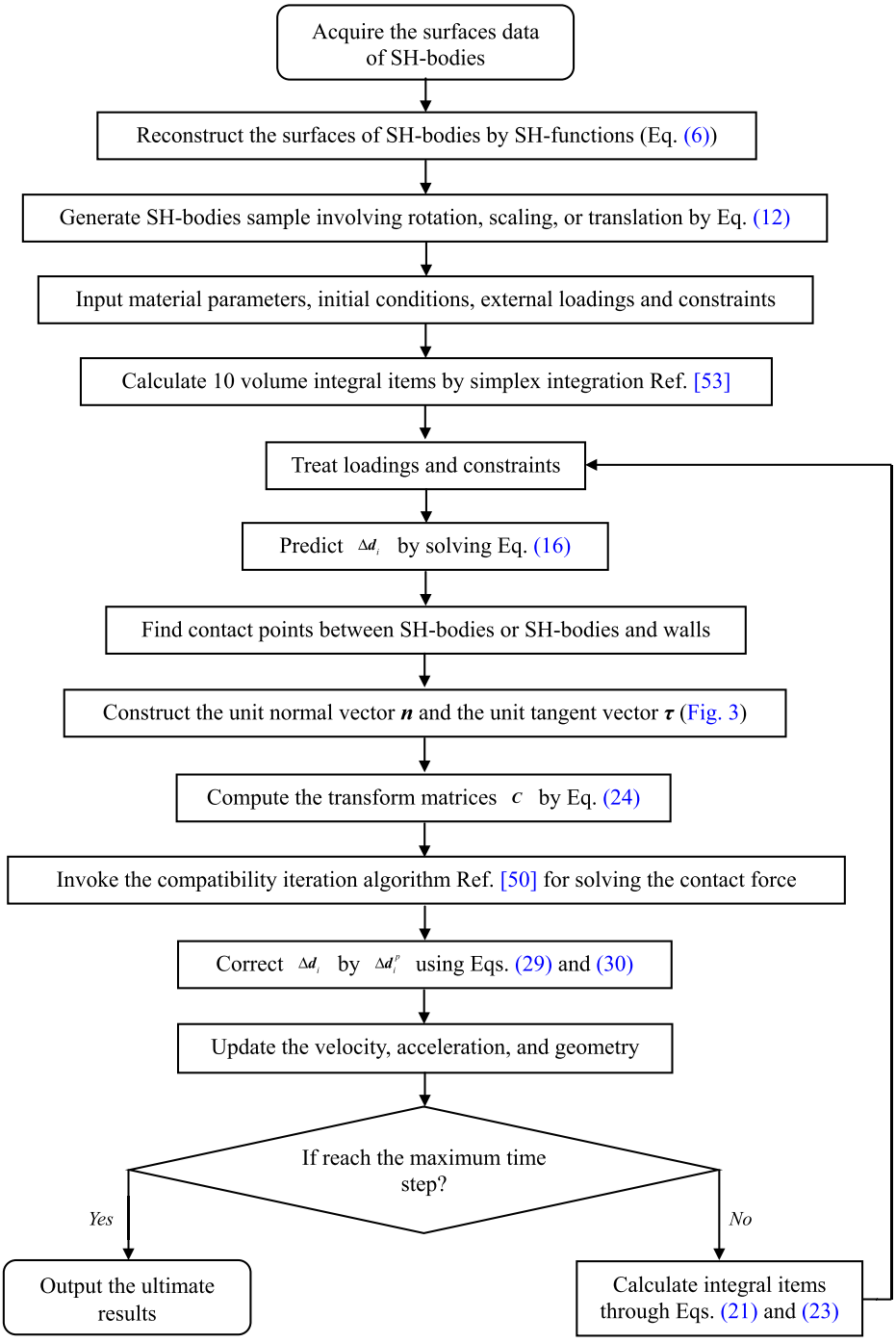

Fig. 18. Flowchart of dynamic modeling of SH-Bodies.

and curvature circle, can be adopted to estimate the iteration increments that are

$$\delta\theta = \lambda_\theta \delta s, \quad \delta\varphi = \lambda_\varphi \delta s \tag{49}$$

where

$$\delta s = \operatorname{sign}(\boldsymbol{c}_k' \cdot \overrightarrow{\mathrm{I}_k\mathrm{A}}) \sqrt{\frac{2\ |\boldsymbol{c}_k' \times \overrightarrow{\mathrm{I}_k\mathrm{A}}|}{|k_n|\,|\boldsymbol{c}_k'|^3}} \tag{50}$$

where sign(·) is the sign function. $\overrightarrow{\mathrm{I}_k\mathrm{A}}$ is a vector from point I_k to point A.

It should be pointed out that the geometric iteration method is a kind of local method. The initial iteration point should generally be determined first. Instead of using infinitely many points, any numerical method uses finitely many points to represent a SH-surface. A triangular or quadrilateral mesh can be generated by these large numbers of points. For convenience of presentation, we take the quadrilateral mesh as an example, as shown in Fig. 8. By comparing the distance between point P and these large numbers of points, we can pick out a point with the minimum distance as the initial iteration point. Assume that point $\mathrm{I}_0(\theta_0, \varphi_0)$ is the initial iteration point (see Fig. 8). Around point I_0, eight points V_1, V_2, …, up to V_8 can be found out with the sampling intervals $\Delta\theta$ and $\Delta\varphi$ along tangent directions $\boldsymbol{r}_{,\theta}$ and $\boldsymbol{r}_{,\varphi}$, respectively. Because point I_0 is the relative closest point to point P among these nine points, therefore, we can limit all iteration points to the zone $\mathrm{V}_1\mathrm{V}_2\mathrm{V}_3\mathrm{V}_4\mathrm{V}_5\mathrm{V}_6\mathrm{V}_7\mathrm{V}_8\mathrm{V}_1$, namely $\theta \in [\theta_0 - \Delta\theta, \ \theta_0 + \Delta\theta]$ and $\varphi \in [\varphi_0 - \Delta\varphi, \ \varphi_0 + \Delta\varphi]$. At the current iteration step, the angles are denoted as $\psi_k(\psi = \theta, \ \varphi)$, we employ the following formulation to estimate the angles ψ_{k+1} for the next iteration step.

$$\begin{cases} \psi_{k+1} = \left[\psi_0 + \Delta\psi - \operatorname{rem}\left(\frac{\psi_0 - \Delta\psi - \bar{\psi}}{2\Delta\psi}\right)\right], & \bar{\psi} < \psi_0 - \Delta\psi \\ \psi_{k+1} = \left[\psi_0 - \Delta\psi + \operatorname{rem}\left(\frac{\bar{\psi} - \psi_0 - \Delta\psi}{2\Delta\psi}\right)\right], & \bar{\psi} > \psi_0 + \Delta\psi \end{cases} \tag{51}$$

where rem(·) is the remainder function, and the interim angle $\bar{\psi}$ is given by

$$\bar{\psi} = \psi_k + \delta\psi, \quad \psi = \theta, \varphi \tag{52}$$

The geometric meaning of Eq. (51) can be illustrated by Fig. 9 indicating that if the interim angle $\bar{\psi} < \psi_0 - \Delta\psi$, then we can use Eq. (51) to make $\psi_{k+1} \in \ [\psi_0, \ \psi_0 + \Delta\psi\ ]$ and $(\psi_0 - \Delta\psi) - \bar{\psi} = (\psi_0 + \Delta\psi) - \psi_{k+1}$ (see the blue dotted line with an arrow in Fig. 9); if $\bar{\psi} > \psi_0 + \Delta\psi$, then Eq. (51) can make $\psi_{k+1} \in \ [\psi_0 - \Delta\psi, \ \psi_0\ ]$ and $\psi_{k+1} - (\psi_0 - \Delta\psi) = \bar{\psi} - (\psi_0 + \Delta\psi)$ (see the purple dotted line with an arrow in Fig. 9). Eq. (51) is a key ingredient for applying the geometric iteration method to a SH-surface. In Section 5, we will test the proposed method.

Note that the SH-surface of any SH-body is closed, if point P is inside of SH-surface, the first- and second geometric iteration algorithms are still available. In this case, however, for the angle control approach, the preset angle tolerance to terminating the iteration should be close to π (180°). If we don't know in advance whether point P is inside or outside of SH-surface, the increment control approach is recommended. If

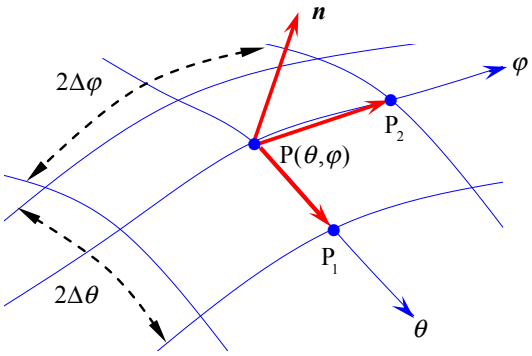

Fig. 19. The relative positions of points P, P_1, and P_2.

Table 1
Some representative sand particles.

Original particles	Reconstructed SH-bodies	Original particles	Reconstructed SH-bodies
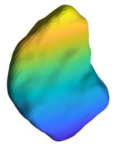	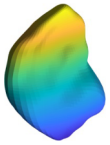	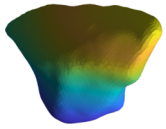	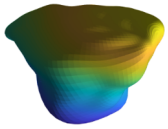
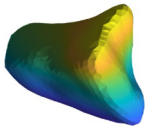	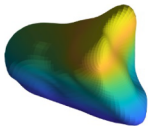	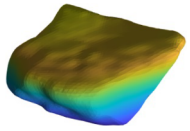	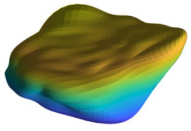
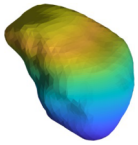	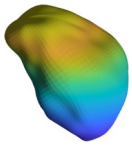	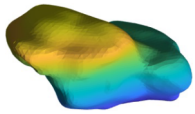	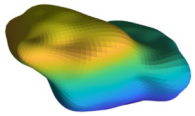
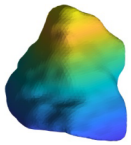	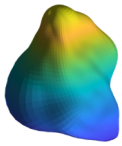	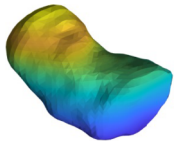	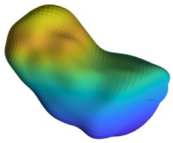
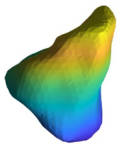	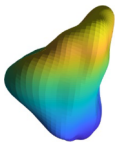	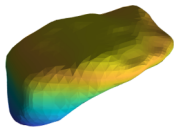	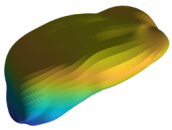

necessary, when the iteration completed the angle between $\overrightarrow{I_kP}$ and normal vector $\boldsymbol{n}$ can be used to judge whether point P is inside or outside of SH-surface.

4.2. The closest points between two SH-bodies

In this section, we will extend the geometric iteration methods for the closest point between point and SH-surface described above to find the closest point between two SH-bodies.

Any individual SH-body has a unique external box (EB) to surround itself for a preliminary check of inter-body contact, as shown in Fig. 10. The external box is defined as a rectangular parallelepiped (or cuboid), of which three orthogonal edges are the projected segments of the SH-body onto x, y, and z axes, respectively (see Fig. 10). Thus, the external box is an axis-aligned bounding box [56] and has been widely used to accelerate the performance of collision detection algorithms.

For two SH-bodies, assume that their EBs are $A_1B_1C_1D_1E_1F_1G_1H_1$ and $A_2B_2C_2D_2E_2F_2G_2H_2$, respectively (see Figure (c) in Fig. 11). Their external overlapping box (EOB) is defined as the intersection between the two EBs, namely the EOB (ABCDEFGH). In order to locate the EOB, vertex E is firstly determined by $E = (E_x, E_y, E_z) = (\max(E_{1x}, E_{2x}), \max(E_{1y}, E_{2y}), \max(E_{1z}\ E_{2z}))$, then the three lengths of the EOB can be estimated by $a = |EH| = \min(H_{1x}, H_{2x}) - E_x$ along x-axis, $b = |EF| = \min(F_{1y}, F_{2y}) - E_y$ along y-axis, and $c = |EA| = \min(A_{1z}, A_{2z}) - E_z$ along z-axis, respectively. If $a \le 0$ or $b \le 0$, or $c \le 0$, we can conclude that the EOB is inexistent. Otherwise, we can get a EOB, whose eight vertexes are defined as: $A(E_x, E_y, E_z + c)$, $B(E_x, E_y + b, E_z + c)$, $C(E_x + a, E_y + b, E_z + c)$, $D(E_x + a, E_y, E_z + c)$, $E(E_x, E_y, E_z)$, $F(E_x, E_y + b, E_z)$, $G(E_x + a, E_y + b, E_z)$, and $H(E_x + a, E_y, E_z)$, as depicted in Figure (d) in Fig. 11.

If an EOB does not exist, then we may draw that the two related SH-bodies do not contact. However, if an EOB does exist, there are two possible cases: two non-overlap SH-bodies and two overlap SH-bodies. For convenience of illustration and observation, here, two dimensional schematics are only given, as displayed in Fig. 12.

In general, an overlap checking procedure should be conducted to identify the two possible cases (see Fig. 12). For this purpose, the distance-based algorithm [57], the contact equation [57], or the separation axis theorem [58] could be employed. However, these methods all seem to be complicated. Note that there is at least one intersection point between two overlap SH-surfaces. From two SH-surfaces, if we can find out a pair of vertices between that the distance is less than an enough small value d_{overlap} (e.g. 1.0×10^{-6}), then we can conclude that the two SH-surfaces overlap with each other. Based on this, we have the following ***overlap checking*** approach (called as the orthogonal projection-

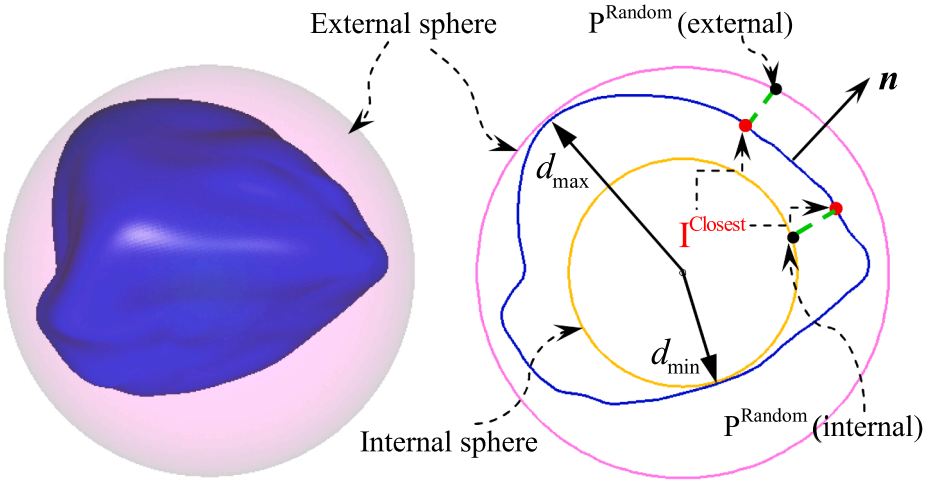

Fig. 20. A SH-body and its external sphere.

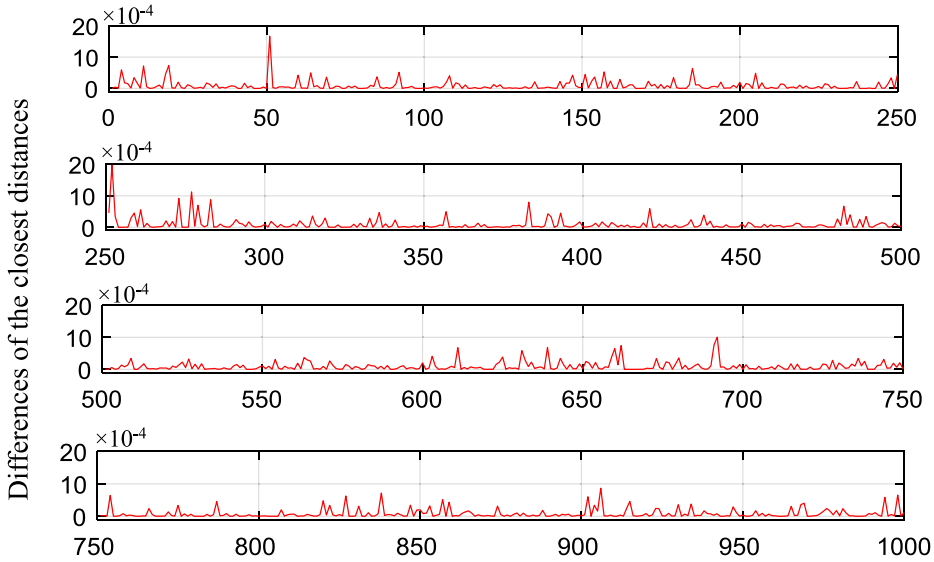

Fig. 21. Differences between closest distances predicted by the first- and second-order algorithms for 1000 random checking points.

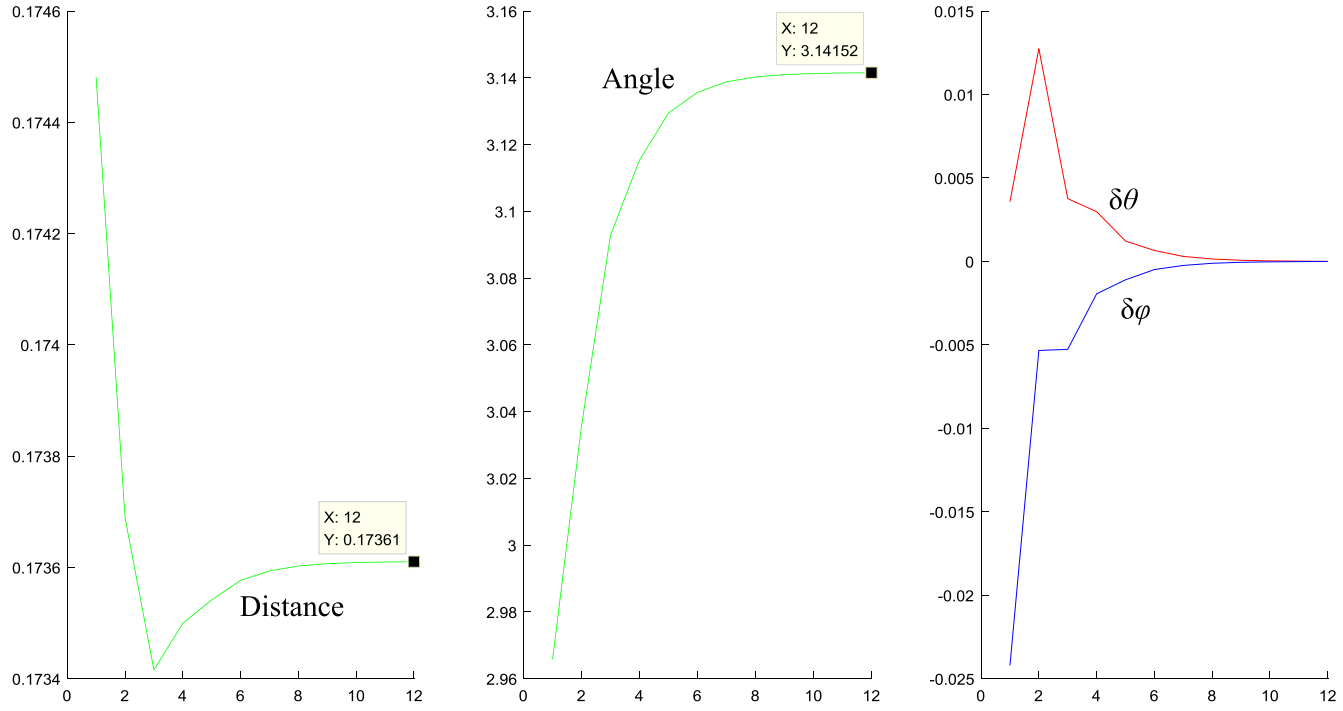

(a) First-order algorithm: iteration steps = 12 (unit of angle: *rad*)

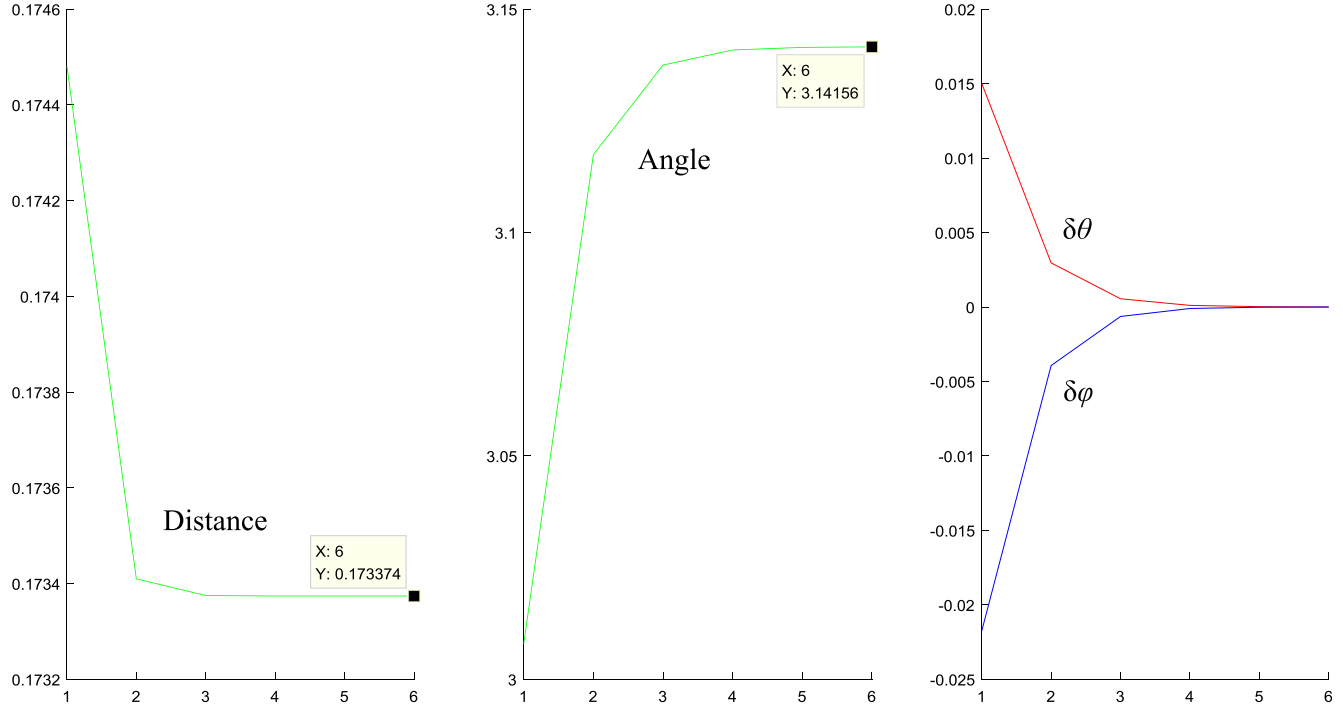

(b) Second-order algorithm: iteration steps = 6 (unit of angle: *rad*)

Fig. 22. Iteration curve of the proposed methods for a random internal checking point.

based algorithm, which is simple and intuitive.):

(1) Calculate EB-*i* and EB-*j* to determine if there is EOB between SH-body-*i* and SH-body-*j*.
(2) If EOB don't exist, shift to consider another pair of SH-bodies.
(3) If EOB do exist,
   (a) From EOB, find out the set of vertices-*i* and the set of vertices-*j*, which are on SH-body-*i* and SH-body-*j*, respectively.
   (b) From the set of vertices-*i* and the set of vertices-*j* pick out a pair of closest vertices, e. g. i_1 and j_1 in Fig. 12. Line i_1j_1 is called the initial iteration line.
   (c) Choose an endpoint of the initial iteration line as the given point P and another endpoint as the initial iteration point I_0 to find the closest point I_k between a point and a SH-surface. Then,

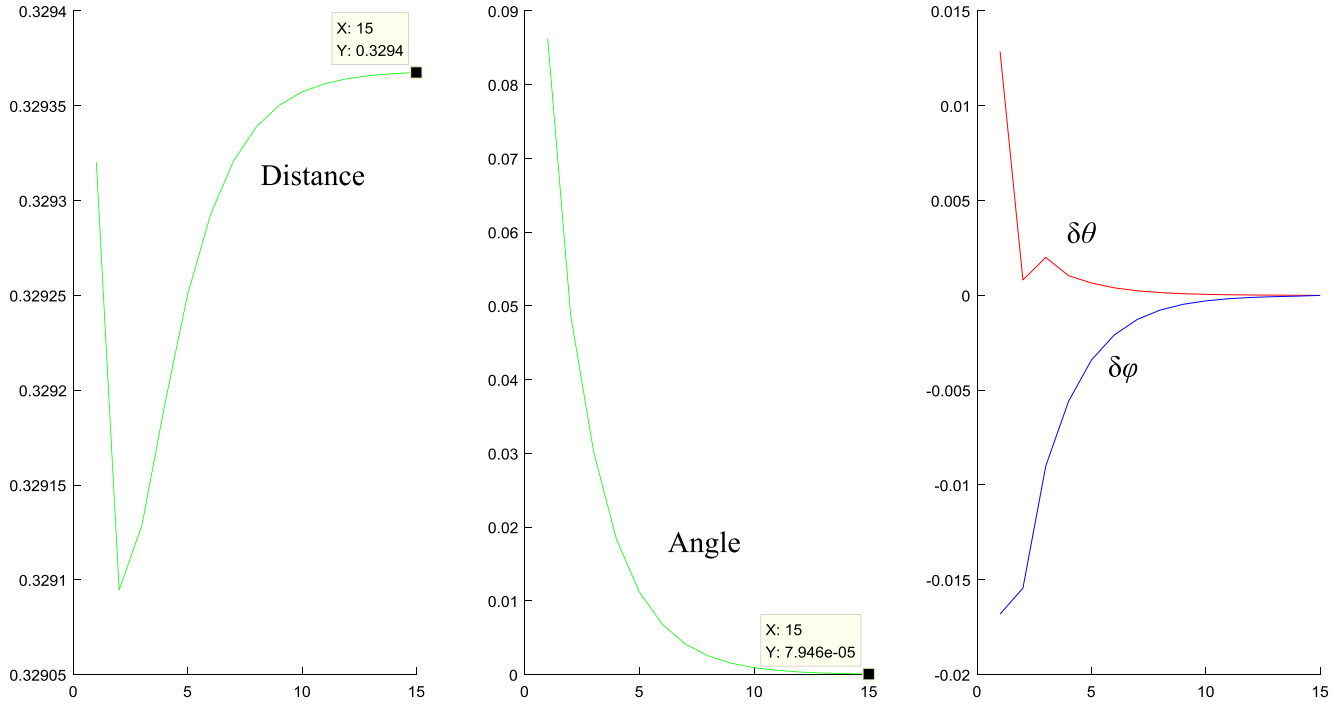

(a) First-order algorithm: iteration steps = 15 (unit of angle: *rad*)

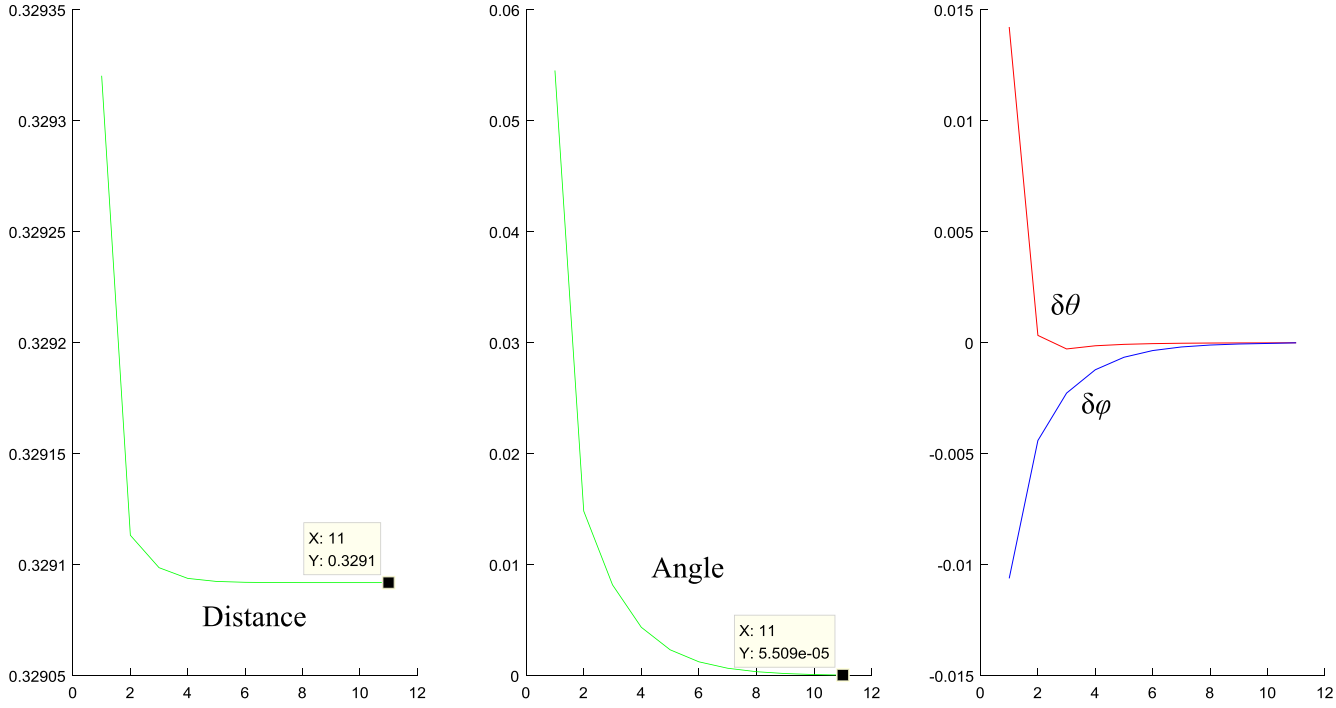

(b) Second-order algorithm: iteration steps = 11(unit of angle: *rad*)

Fig. 23. Iteration curve of the proposed methods for a random external checking point.

we take point I_k as the new initial iteration point for the next geometric iteration. Usually, after several time repeats we can get a common perpendicular line AB to the two SH-bodies, see Fig. 13.

(d) If the distance d between point pair A-B is more than $d_{overlap}$ (e.g. 1.0×10^{-6}), it is the case of two non-overlap SH-bodies (Fig. 13(a)); otherwise, it is the case of two overlap SH-bodies (Fig. 13(b)).

It should pointed out that there may exist multi-point pairs, e. g. A_1-B_1, A_2-B_2,.., the corresponding distances d_1, d_2, … between each of point pairs are all more than $d_{overlap}$, meanwhile, these distances are almost equal to each other. Namely, there exist multi-non-overlap regions. In this case, we should deal with these non-overlap regions one by one using the following contact determining algorithm to find out multi-contact pairs.

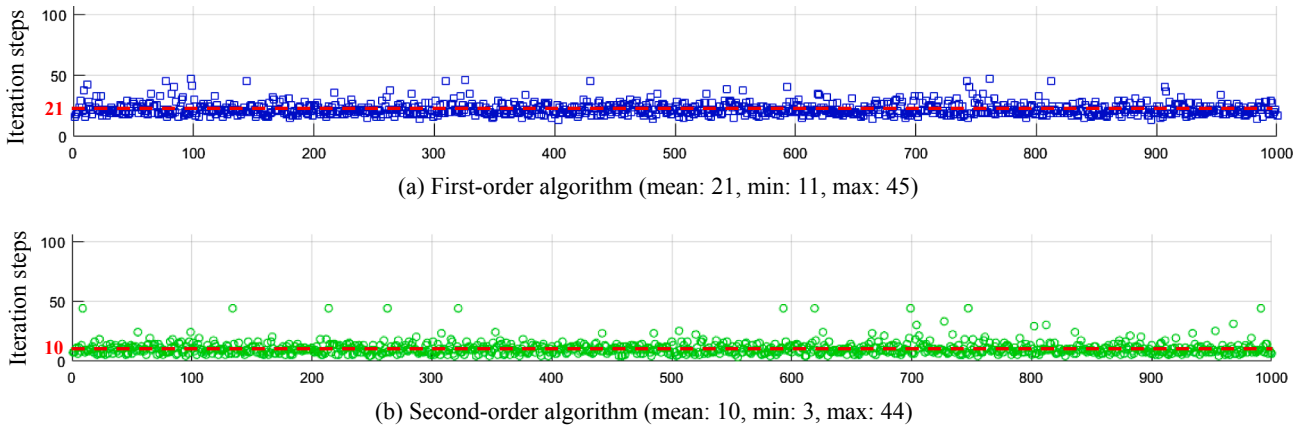

Fig. 24. Iteration steps of the proposed method for 1000 random checking points.

After distinguishing the two cases, we can subsequently perform the following ***contact determining*** algorithm to dispose the non-overlap case firstly:

(1) For the case of two non-overlap SH-bodies, the common perpendicular line AB (see Fig. 13(a)) severs as the normal contact line AB. And the direction of normal contact is defined as from the SH-body with a smaller global index to the SH-body with a bigger global index (assume $i < j$, see *red* solid lines in Fig. 13(a)). Correspondingly, the mid-point of the normal contact line AB is divided into two contact points C_1 and C_2, which belong to SH-body-*i* and SH-body-*j*, respectively.
(2) Determine the direction of tangent contact according to the pre-estimated (without considering the contact force) relative displacement of the two contact points C_1 and C_2 (referred to Section 3.2 for more details).

Before further dealing with the case of two overlap SH-bodies, we would like to scrutinize closely on the widely-used tactic adopted by the contact function method [59,60], the common plane method [61,62], the geometric potential method [63], and the common normal algorithm [64] in order to reveal its logics. The contact function method takes the intersection line of two SH-surfaces as the tangent contact line, whose mid-point serves as the contact point. For the common plane method, its normal vector is chosen as the contact normal vector. The tangent contact line is on the common plane (see Fig. 14). While in the geometric potential method, one should firstly find out the minimum geometric potential line, which is regarded as the contact normal line whose mid-point is defined as the contact point. As for the common normal method, two specific points on each of two SH-surfaces are found in a condition such that the normal directions at these points are parallel to the line that passes through the two points. The mid-point of the common line is specified as the contact point, as described in Fig. 14. Obviously, the contact points and the contact directions provided by these methods are not necessarily the same. However, the starting point behind them is exactly identical: firstly, let two SH-surfaces overlap each other; and then, based on the overlap region to define the contact point and the contact directions. Thus, we can call this approach as the "overlap-based" scheme. Realistically, the overlap between two rigid bodies in contact is not allowed. Computationally, the displacement of any individual body is a small value within a time increment. To address the contact corresponding to the case of two overlap SH-bodies, we employ a different strategy (referred to as "separation-based" scheme), as illustrated in Fig. 15.

If there is at least one intersection point between two SH-surfaces (see the overlap checking algorithm), the following "separation-based procedure" should be performed to "push" the two bodies to their respective temporary locations, i.e. SH-body-*i** and SH-body-*j**.

(1) Change the positions of the two bodies by $-k\Delta\boldsymbol{d}_i^{\text{last}}$ and $-k\Delta\boldsymbol{d}_j^{\text{last}}$, where $\Delta\boldsymbol{d}_i^{\text{last}}$ and $\Delta\boldsymbol{d}_j^{\text{last}}$ are the increments of DOFs of the two bodies within the last time step. The coefficient k (recommended value $k \in [0.3, 0.7]$) is a positive real number. In current study, we set $k = 0.4$. The negative sign $(-)$ indicates that the "separation-based" scheme is a reverse "operation".
(2) Invoke the overlap checking algorithm to determine whether there is at least one intersection point between the two SH-surfaces.
(3) Repeat the steps (1) and (2) until the two SH-bodies have been separated.
(4) Call the contact determining algorithm to obtain the temporary contact line A* (θ_A, φ_A) B* (θ_B, φ_B), which belong to SH-body-*i** and SH-body-*j**, respectively, see Fig. 15.

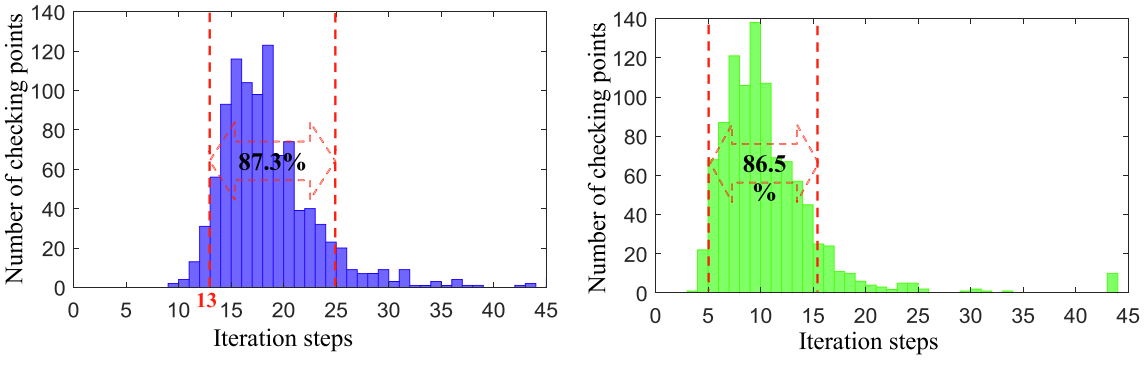

Fig. 25. Histograms of iteration steps for 1000 random checking points.

(5) Determine the contact line AB on SH-body-i and SH-body-j according to two sets of angle parameters (θ_A, φ_A) and (θ_B, φ_B), respectively. Then, the contact point C and the contact direction can be obtained easily.

Usually, we can successfully separate the two bodies within two or three cycles. Moreover, the usage of the separation-based scheme can avoid some difficulties that might exist in the overlap-based scheme, such as the increment of computation cost, the degradation of stability, the decrement of accuracy, and even calculation failure, especially for handling two highly complex SH-surfaces. In addition, the separation-based scheme is more in line with the physical reality.

We know that a plane with the normal vector $\boldsymbol{n}$ can be determined by points A, B, and C, as shown in Fig. 16. An arbitrary point P(x, y, z) on this plane is given by

$$\begin{cases} x = x_A + (x_B - x_A)\lambda + m\mu \\ y = y_A + (y_B - y_A)\lambda + n\mu \\ z = z_A + (z_B - z_A)\lambda + p\mu \end{cases} \tag{53}$$

where λ and μ are the parameters. Vector $\boldsymbol{\tau}(m, n, p)$ is the direction vector of line BC. Using the following pseudo-code, we can generate $(N + 1)\times(N + 1)$ points distributing uniformly on this plane, as sketched in Fig. 17.

```
Δ = |AB|/N;
i = −1;
for(x = 0; x ≤ |AB|; x + = Δ)
  for(y = 0; y ≤ |AB|; y + = Δ)
    point[++i] = A + (B − A) * x + τ * y;
```

where |AB| is the length of edge AB.

Obviously, only these points that are in the triangle ABC will be likely to be valid contact points. We can further use existing open source code [65] to identify these points.

Then, the overlap checking approach, the contact determining algorithm, and the separation-based procedure can be extended easily to deal with the contact between plane and SH-surface.

For the sake of convenience, the main process of conducting dynamic simulation is summarized in Fig. 18.

5. Numerical examples

In this section, we will compare the first-order and second-order algorithms. Then, the validity of SH-body-based DDA (abbreviated as SHB-DDA) will be demonstrated.

Table 1 shows some representative real sand particles and the corresponding reconstructed ones that will be used to examine the relevant algorithms. Moreover, instead of using fixed springs, which maybe induce additional energy, we assign a huge value of material density to a rigid body that is desired to be stationary. Compatibility iteration [50]

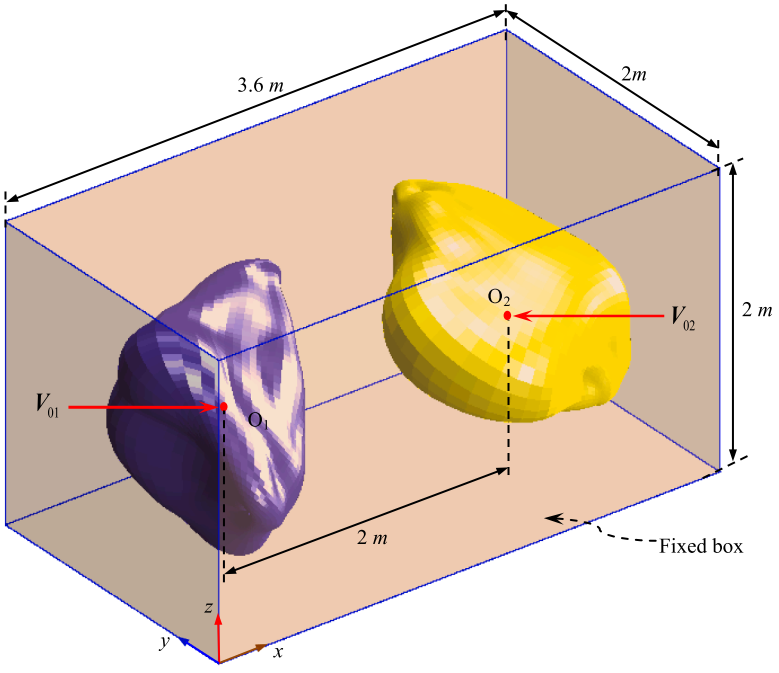

(a) 3D view

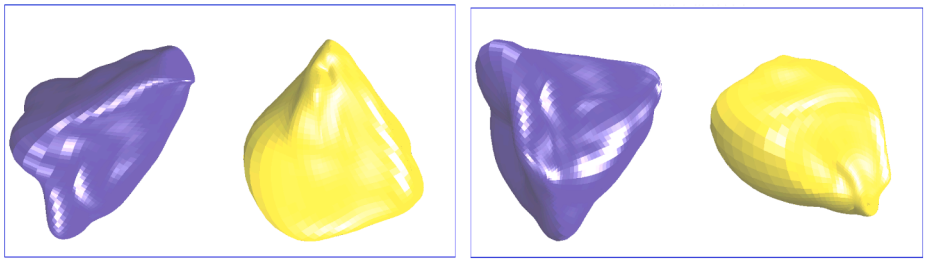

(b) 2D view-1 (c) 2D view-2

Fig. 26. Initial configuration of two SH-bodies.

is used to calculate the contact force. Moreover, to reduce computational cost, the unit normal vector at any point P(θ, φ) is approximated by

$$\boldsymbol{n} = \frac{\overrightarrow{PP_1} \times \overrightarrow{PP_2}}{|\overrightarrow{PP_1} \times \overrightarrow{PP_2}|} \tag{54}$$

where points P_1 and P_2 are both very near to point P. The relative positions of points P(θ, φ), $P_1(\theta + \Delta\theta/10^8, \varphi)$, and $P_2(\theta, \varphi + \Delta\varphi/10^8)$ are sketched in Fig. 19.

5.1. Test of the closest point from point to SH-surface

Before testing, for the sake of generality, the vertices of a SH-body are firstly scaled to a unit sphere through the following procedure: (1) Determine the farthest distance d_{max} between these vertices and the center of the SH-body; (2) Calculate three scaling factors $S_x = S_y = S_z = 1.0/d_{max}$; (3) Scale these vertices by S_x, S_y, and S_z taking the centroid of the SH-body as the scaling center. Then, the SH-body's *external sphere* with the radius $r = 1.0$ can be constructed, as shown in Fig. 20. Further, the nearest distance d_{min} between these new vertices and the center of the SH-body can be evaluated to generate the SH-body's *internal sphere* with the radius $r = d_{min}/d_{max}$. In order to test the algorithm for finding the closest point between a point and the SH-surface, 1000 random checking point P^{Random} will be generated randomly on the internal or external spheres, respectively. Assume that the unit normal vector $\boldsymbol{n}$ of the SH-surface is outward. The target of the geometric iteration algorithm is to find out the closest point $I^{Closest}$. Set the maximum number of iterations is to be 50. And the other iteration termination conditions are $\delta\theta \le 1.0 \times 10^{-5}$ *rad* and $\delta\varphi \le 1.0 \times 10^{-5}$ *rad*. Some results are shown in Figs. 21–25.

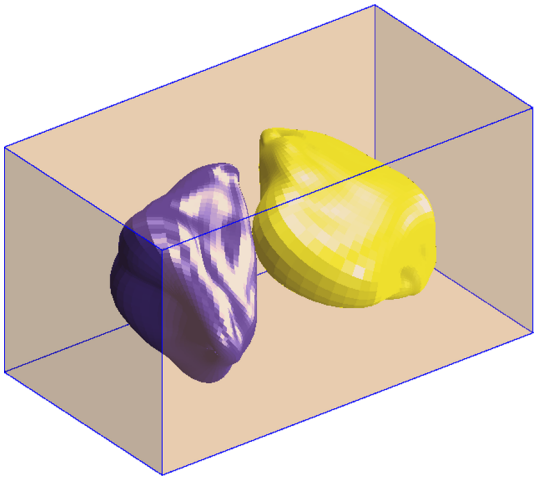

Fig. 27. Configuration (TS = 300) of two SH-bodies.

For the 1000 random checking points, the differences between the closest distances obtained from the two proposed methods are sketched in Fig. 21, in which the fluctuation of the red line indicates that there are differences between the closest distances given by the two methods. Upon closer examination, we find that the maximum difference between the two sets of data is about equal to 0.0020, which is an error that cannot be ignored in the contact analysis of rigid particle in our experiences. Next, we will take two random checking points for an example to demonstrate the iteration process of the two methods.

We first observe the iteration process of a random internal point. This means that the angle between vector $I^{Closest}\overrightarrow{P^{Random}}$ and normal vector $\boldsymbol{n}$ should be close to π ($\approx 3.14159\,rad$) when the iteration achieves to convergence. For the first-order algorithm, the corresponding iteration curves are presented in Fig. 22. As $\delta\theta$ and $\delta\varphi$ both approach to 1.0×10^{-5}, compared with the first-order algorithm and the first-order algorithm, the angles are about equal to 3.14152 *rad* and 3.14156 *rad*, respectively. Meanwhile, the closest distances obtained are about 0.1736 and 0.1733, respectively. While the iteration steps are 12 and 6, respectively. This is to say that the second-order algorithm enjoys a faster convergence speed ($6 < 12$) and a higher computational accuracy ($0.1733 < 0.1736$) then the first-order algorithm.

Now, we scrutinize the iteration process of a random external point. This is to say that the angle between vector $I^{Closest}\overrightarrow{P^{Random}}$ and unit normal vector $\boldsymbol{n}$ should be close to 0 when the iteration is completed. For the first-order algorithm, as we can see from Fig. 23(a) and (b), along with the decrements of $\delta\theta$ and $\delta\varphi$, the angle approaches gradually to 0. Meanwhile, the closest distances are about equal to 0.3294 and 0.3291, respectively. Moreover, the iteration steps are 15 and 13 corresponding to the first- and second-order algorithms, respectively. Similar to the previous case of a random internal point, generally, in terms of computational accuracy and convergence speed, the second-order algorithm has the better performance. For more clearly explain this point, the corresponding iteration steps of the 1000 random points are further summarized in Figs. 24 and 25.

For the 1000 random checking points, the iteration steps of the proposed methods are demonstrated statistically in Fig. 24. For the first-order algorithm, by calculating the mean, minimum, and maximum of the iteration steps are 21, 11, and 45 (Fig. 24(a)), respectively. For the

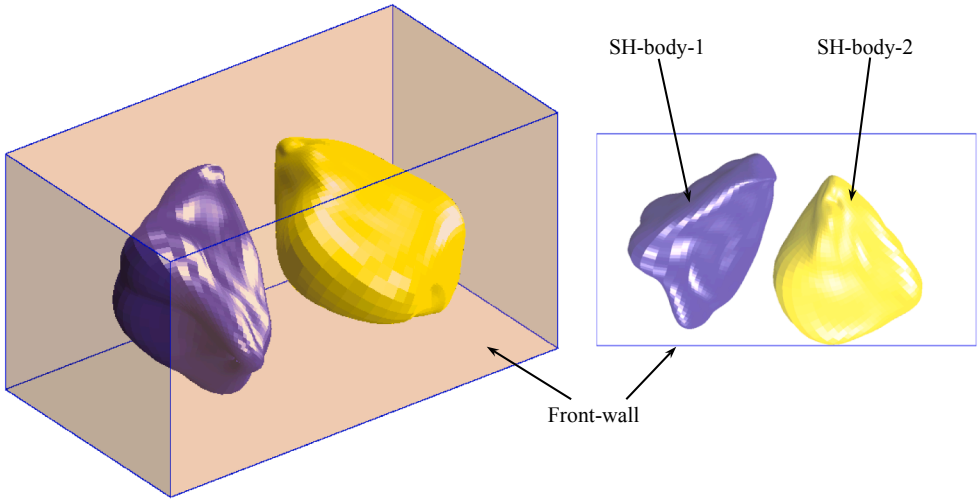

Fig. 28. Configuration (TS = 400) of two SH-bodies.

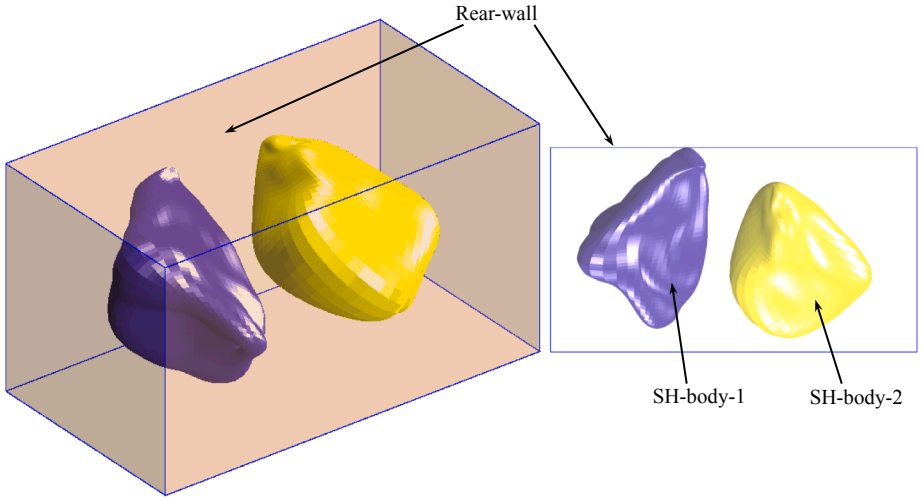

Fig. 29. Configuration (TS = 550) of two SH-bodies.

second-order algorithm, on the other hand, they are equal to 10, 3, and 44 (Fig. 24(b)), respectively. These data reveal that the second-order is superior to the first-order one.

The iteration steps corresponding to the 1000 random checking points are illustrated statistically in Fig. 25. From the two histograms, we can find that the majority checking points (i.e. 87.3%) whose iteration steps associated with the first-order algorithm is about in between 13 and 25. Meanwhile, for the second-order algorithm, there are the majority checking points (i.e. 86.5%) whose iteration steps are roughly in between 5 and 15. It is suggests that the second-order

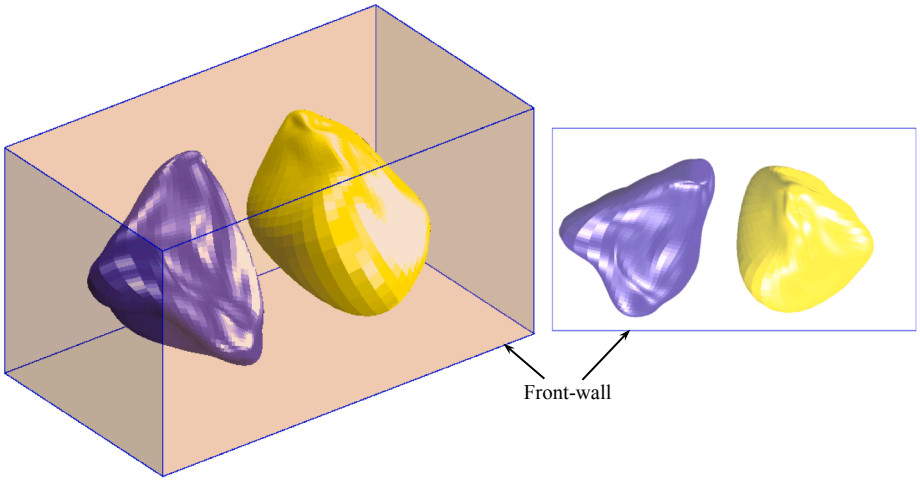

Fig. 30. Configuration (TS = 800) of two SH-bodies.

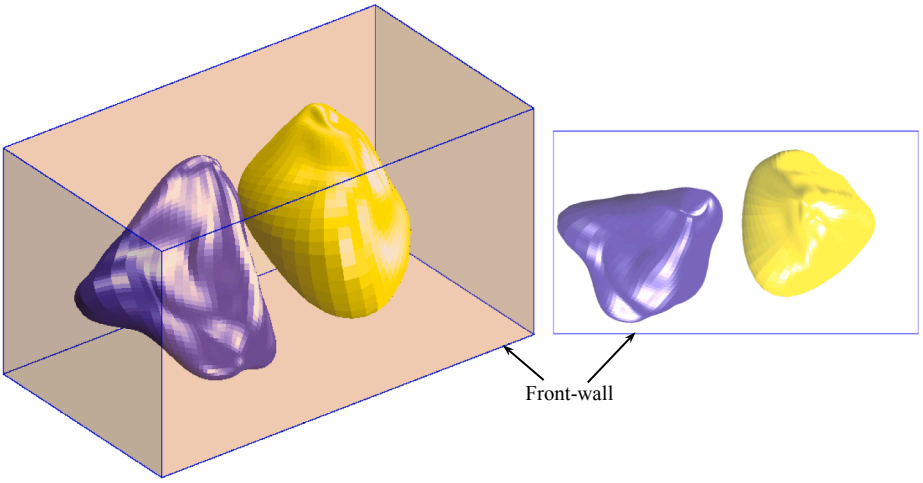

Fig. 31. Configuration (TS = 1000) of two SH-bodies.

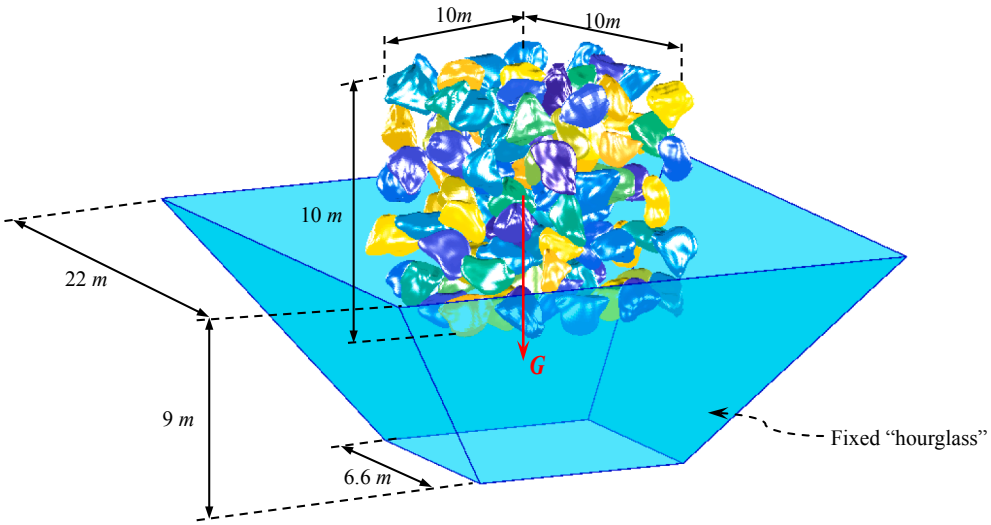

(a) 3D view-1

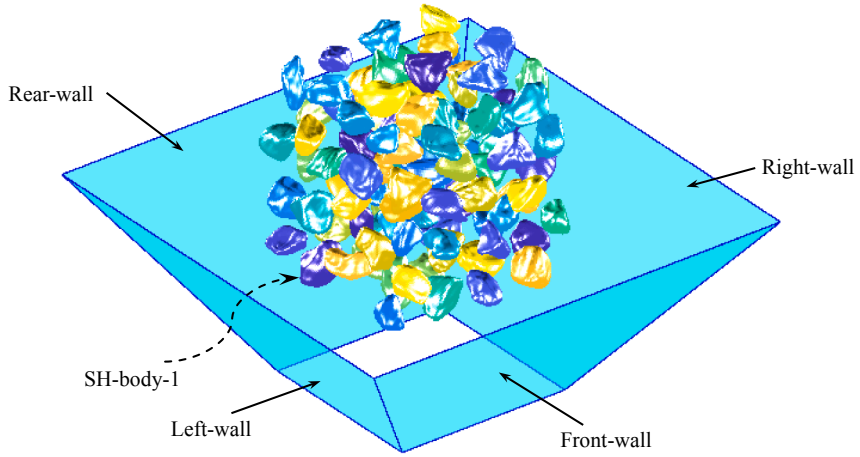

(b) 3D view-2

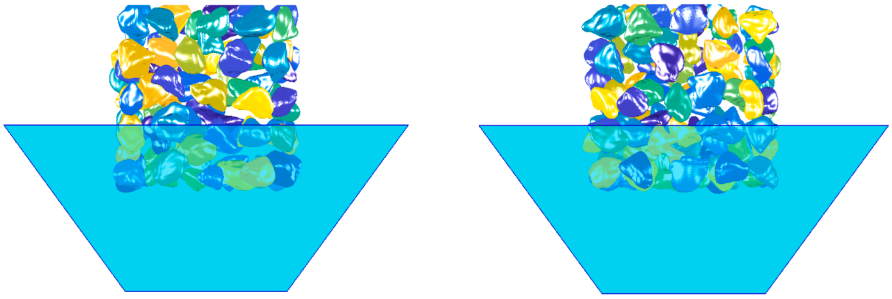

(c) 2D view-1 (d) 2D view-2

Fig. 32. Initial configuration of a group of random SH-bodies.

algorithm is recommendable. From Fig. 25, it is can be found that there are very small amount of checking points (< 1%), whose iteration steps are up to 44 or 45. On scrutiny, we further find that the closest points on the SH-surface corresponding to these checking points are almost always concave points with relative larger curvatures, which mean that at these points the SH-surface bend towards its interior in a relative steep way. These points are unlikely to be contact points between two SH-bodies. All in all, the extended geometric iteration algorithms has good convergence for a majority of cases, and the second-order algorithm is shown to be superior to the first-order one.

5.2. Interaction of two SH-bodies

Based on comparison done in the previous section, the second-order algorithm will be employed to further demonstrate the effectiveness of the method. In the followings, we design two complex examples. One can refer to Section 3.2 for more details about handling of contact forces. The treatment of loads and inertia is the same as that in original DDA. During the simulation, we will pick out some results at representative time steps to show the motion of SH-bodies.

Firstly, the motion of two SH-particles in a fixed box with dimensions $3.6 \times 2.0 \times 2.0\,\mathrm{m}^3$ is simulated. The two SH-particles are both

scaled to the unit sphere, as shown in Fig. 26. Initially, the distance between their centers O_1 and O_2 is equal to 2 m. Set the initial velocities $\boldsymbol{V}_{01} = -\boldsymbol{V}_{02} = (1.0, 0.0, 0.0)$ *m/s*, which means that the two SH-bodies will move towards each other in the opposite directions at the beginning of simulation. Moreover, the size of time step is to be 0.001 s, and the total time step (TS) is 1000. In this example, the gravity is not considered. Note that the choice of these numerical values is just for demonstrating purpose. For the proposed methods itself, there is no limitation on the choices of the box size and initial velocities. Some results are illustrated in Figs. 27–31.

As TS = 300, the two SH-bodies are just in contact with each other, as presented in Fig. 27. Then, under the action of the contact force and the inertia, the two SH-bodies are separated. Meanwhile, from this moment they have no-zero angle velocity, which means that the two SH-bodies will undergo the composite motion including the translation and rotation.

When TS = 400, SH-body-2 touches with the front-wall of the fixed box, as depicted in Fig. 28. While SH-body-1 continues to move without subjecting to any external force.

While TS = 550, SH-body-1 contacts with the rear-wall of the fixed box, as indicated in Fig. 29. At the same time, SH-body-2 continues to move freely. For TS = 800, 1000, the position of the two SH-bodies are displayed in Figs. 30 and 31, respectively.

5.3. Motion of a group of random SH-bodies

Fig. 32 shows a group of random SH-bodies (outline dimension: $10.0 \times 10.0 \times 10.0\,m^3$, and 10.0 m is identified the characteristic length for convenience of presentation) that are generated randomly according to the sample SH-bodies listed in Table 1. To generate random SH-bodies sample, statistical information about morphologies and characteristics of nature sands or bodies should be taken in to account [35,36,66]. One can further refer to [67,68] for considering the influence induced by parameter uncertainty.

Under the action of the gravity, these SH-bodies will fall into the bottom fixed “hourglass”, which is a frustum without the upper and bottom surfaces. The edge length of the upper surface is equal to 22 m, while for the bottom surface the edge length is 6.6 m. And the high is equal to 9 m, as indicated in Fig. 32(a). In this example, the size of time step is to be 0.001 s, and the total time step (TS) is 2000. Some results are exhibited in Figs. 33–37.

Along with the advance of time, when TS = 850, SH-body-1 just contacts with the left-wall of the hourglass, as shown in Fig. 33, and is ready to rebound. While the other SH-bodies continue falling downwards.

At TS = 890, SH-body-2 touches with the front-wall of the hourglass, as exhibited in Fig. 34. At the next time step, it will rebound under the relevant contact force. Moreover, there are interaction between SH-body-1 and the others around it.

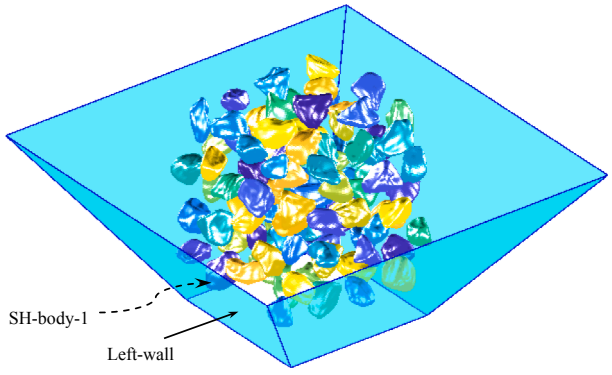

Fig. 33. Configuration of a group of random SH-bodies at TS = 851.

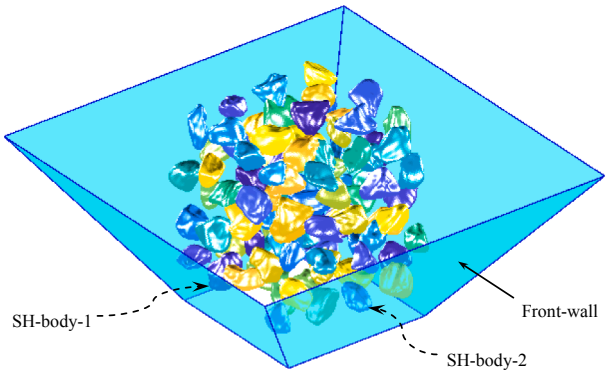

Fig. 34. Configuration of a group of random SH-bodies at TS = 890.

On one hand, the edge length (6.6 m) of the bottom open of the hourglass is less than the characteristic length (10.0 m) of the group of SH-bodies, these SH-bodies on the bottom layer will first meet obstacle during their descent. On other hand, these SH-bodies on the upper layer are still free falling. Thus, about before TS = 1240, the group of random SH-bodies that are relative loose at the initial time become relative density little by little, as illustrated in Fig. 35.

When the group of random SH-bodies are more and more density, the interactions between SH-bodies tend to be more intense. Therefore, about after TS = 1240, these SH-bodies start to be scattered due to the repulsive contact forces, as displayed in Fig. 36.

Next, we pick out 12 SH-bodies to track their movements. At

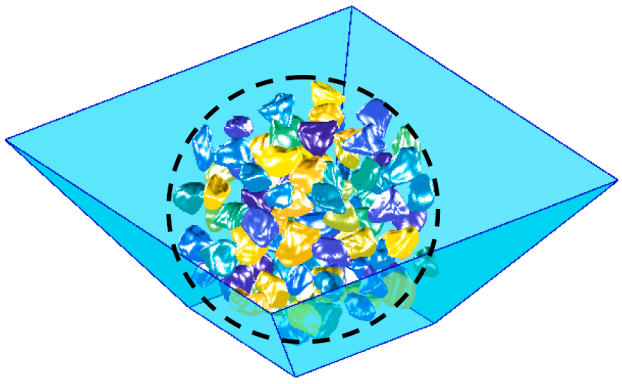

(a) TS = 1000

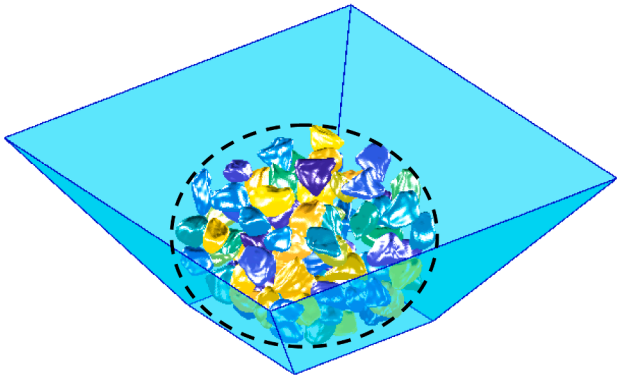

(b) TS = 1240

Fig. 35. Configurations of a group of random SH-bodies from TS = 1000 and TS = 1240.

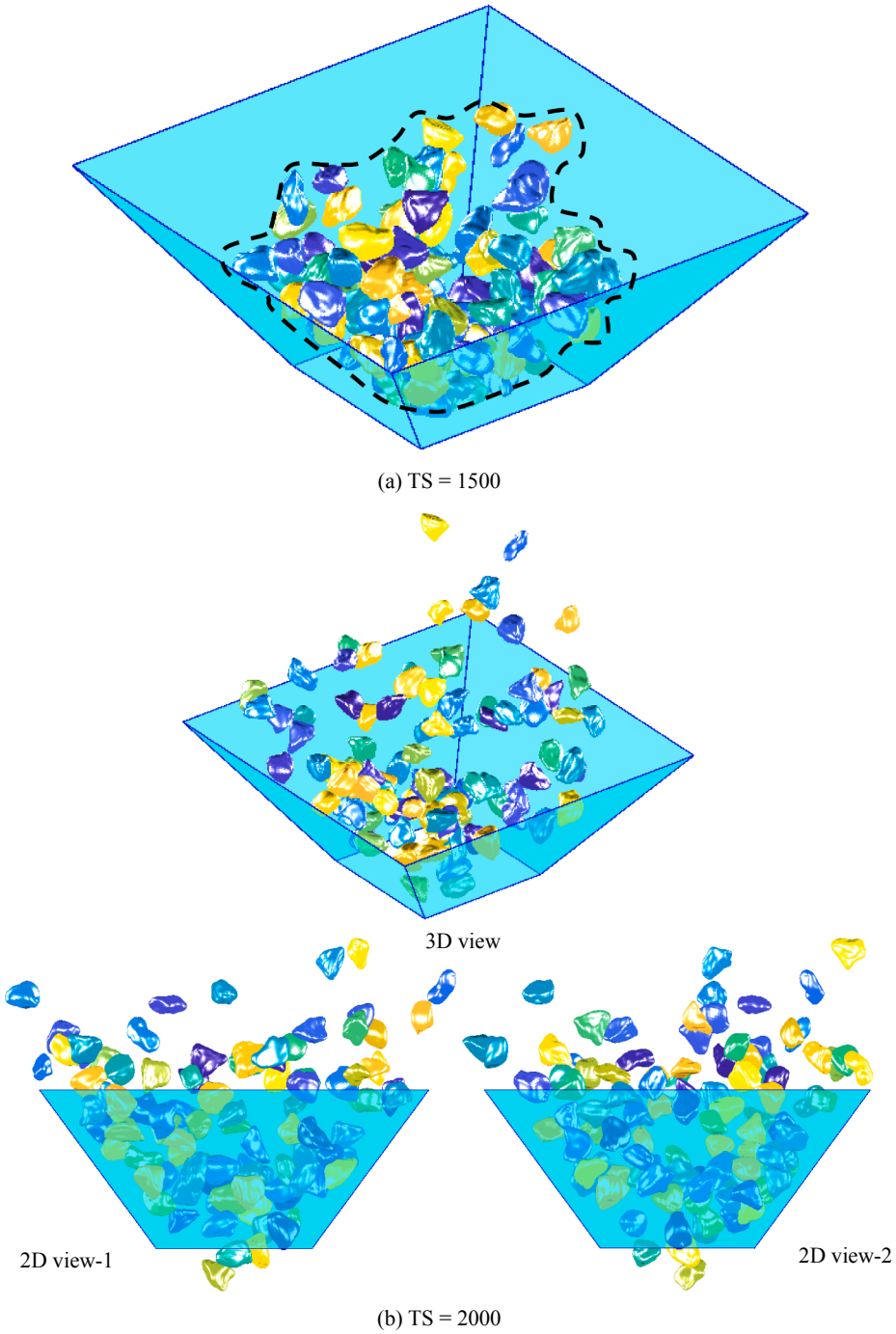

Fig. 36. Configurations of a group of random SH-bodies from TS = 1500 and TS = 2000.

TS = 0, 1300, and 2000, their positions and the trajectories of their centers are presented in Fig. 37, respectively. For ease of observation, we adopt the same color for a SH-body and its trajectory of its center. In Figs. 35 and 36, we have noted that about TS = 1240 the group of SH-bodies start to be scattered upward. Thus, about before TS = 1240 the trajectories are 12 vertical lines, see Fig. 37. Because the shapes of SH-bodies are complex and the initial configuration is not in a dense state, the bounces of these 12 SH-bodies are not synchronous, as shown in Fig. 37. This example demonstrates the ability of the SHB-DDA to capture the motion of multiple SH-bodies.

6. Conclusions

The surface of star-shaped object, either nature or artificial, can be reconstructed by using the spherical harmonic functions to resulting the so-called SH-body. In order to make full use of the analytical properties of the reconstructed surface, a framework for modeling the kinematics and kinetics characteristics of SH-bodies has been established. In the proposed framework, the discontinuous deformation analysis was employed to formulate the governing equation of motion of individual SH-body. Meanwhile, an extended second-order geometric iteration

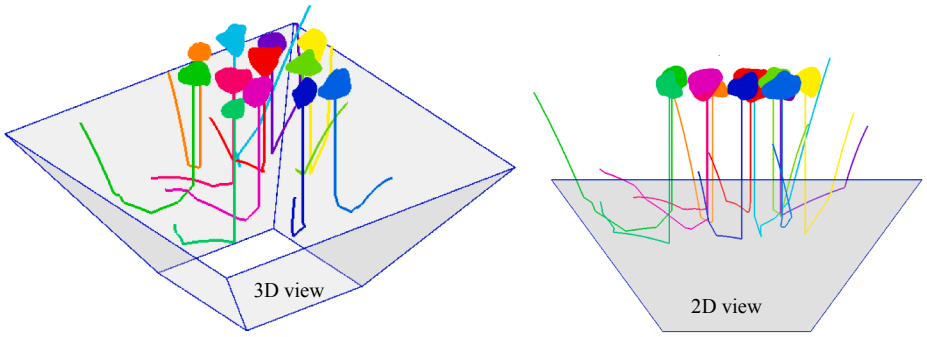

(a) 12 SH-bodies and trajectories of their centers at TS = 0.

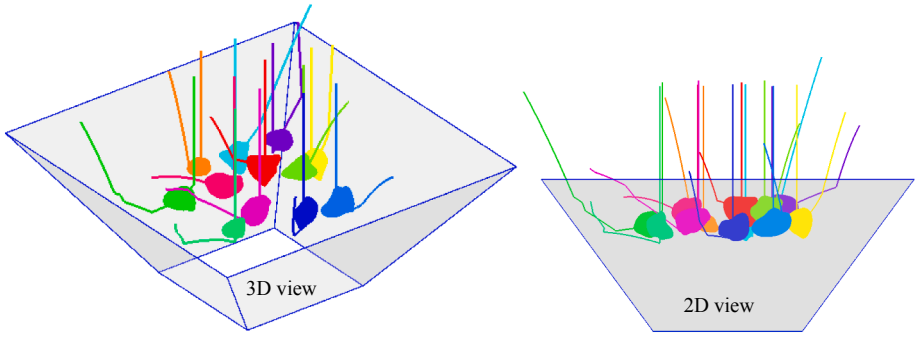

(b) 12 SH-bodies and trajectories of their centers at TS = 1300.

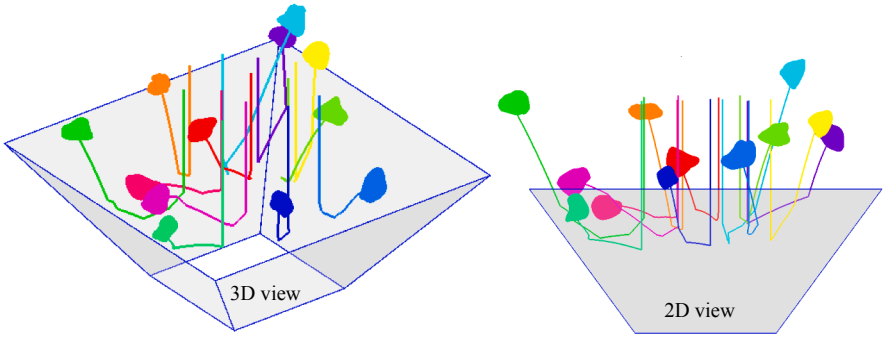

(c) 12 SH-bodies and trajectories of their centers at TS = 2000.

Fig. 37. Configurations of 12 SH-bodies came from the top-level.

algorithm was adopted to identify the contact points between SH-surfaces. To ensure the conservation of energy and momentum, the contact forces were determined by solving the equivalent problem of variational inequality being suitable for the three-dimensional cases. The validation of proposed methodology was demonstrated by several examples. This demonstrates that the new framework will have a broad application prospect.

Acknowledgements

The study is supported by National Key Research and Development Program grant No. 2018YFC0406806 from Ministry of Science and Technology of China, and research grants N_HKUST621/18, 16204618, T22-603-15N from Hong Kong Research Grants Council.

References

[1] Elliott JC, Dover SD. X-ray microtomography. J Microscopy 1982;126(2):211–3.
[2] Flannery BP, Deckman HW, Roberge WG, et al. Three-dimensional X-ray microtomography. Science 1987;237(4821):1439–44.
[3] Stock SR. X-ray microtomography of materials. Int Mater Rev 1999;44(4):141–64.
[4] Landis EN, Keane DT. X-ray microtomography. Mater Charact 2010;61(12):1305–16.
[5] Herman GT. Image reconstruction from projections: the fundamentals of computerized tomography. New York: Academic Press; 1980.
[6] Zhao B, Wang J. 3D quantitative shape analysis on form, roundness, and compactness with μCT. Powder Technol 2016;291:262–75.
[7] Lorensen WE, Cline HE. Marching cubes: a high resolution 3D surface construction algorithm. Comput Graph 1987;21(4):163–9.
[8] Doi A, Koide A. An efficient method of triangulating equi-valued surfaces by using tetrahedral cells. IEICE Trans Inform Syst 1991;74(1):214–24.
[9] Field DA. Laplacian smoothing and Delaunay triangulations. Commun Appl Numer Methods 1988;4(6):709–12.
[10] Stalling D, Zöckler M, Hege HC. Interactive segmentation of 3D medical images with subvoxel accuracy. In: Proc. CAR'98 Computer Assisted Radiology and Surgery; 1998.
[11] Sethian JA. Level set methods and fast marching methods: evolving interfaces in computational geometry, fluid mechanics, computer vision, and materials science. Cambridge University Press; 1999.
[12] Osher S, Fedkiw R. Level set methods and dynamic implicit surfaces. Springer Science & Business Media; 2006.
[13] Kawamoto R, Andò E, Viggiani G, et al. Level set discrete element method for three-dimensional computations with triaxial case study. J Mech Phys Solids 2016;91:1–13.
[14] Vlahinić I, Andò E, Viggiani G, et al. Towards a more accurate characterization of granular media: extracting quantitative descriptors from tomographic images. Granular Matt 2014;16(1):9–21.
[15] Li C, Xu C, Gui C, et al. Distance regularized level set evolution and its application to image segmentation. IEEE Trans Image Process 2010;19(12):3243–54.
[16] Piegl L, Tiller W. The NURBS book. second ed. Berlin: Springer-Verlag; 1997.
[17] Hoschek J, Lasser D. Fundamentals of computer aided geometric design. Wellesley, MA: A.K. Peters; 1993.
[18] Yoo DJ. Three-dimensional surface reconstruction of human bone using a B-spline based interpolation approach. Comput Aided Design 2011;43(8):934–47.
[19] Weiss V, Andor L, Renner G, et al. Advanced surface fitting techniques. Comput

Aided Geom Design 2002;19(1):19–42.
[20] Müller C. Spherical harmonics. Springer; 2006.
[21] https://brilliant.org/wiki/spherical-harmonics/.
[22] Ritchie DW, Kemp GJL. Fast computation, rotation, and comparison of low resolution spherical harmonic molecular surfaces. J Comput Chem 1999;20(4):383–95.
[23] Chung MK, Shen L, Dalton KM, et al. Multi-scale voxel-based morphometry via weighted spherical harmonic representation. International Workshop on Medical Imaging and Virtual Reality. Berlin, Heidelberg: Springer; 2006. p. 36–43.
[24] Max NL, Getzoff ED. Spherical harmonic molecular surfaces. IEEE Comput Graphics Appl 1988;8(4):42–50.
[25] Duncan BS, Olson AJ. Approximation and characterization of molecular surfaces. Biopolym: Orig Res Biomolecul 1993;33(2):219–29.
[26] Brechbühler C, Gerig G, Kübler O. Parametrization of closed surfaces for 3-D shape description. Comput Vision Image Understand 1995;61(2):154–70.
[27] Garboczi EJ. Three-dimensional mathematical analysis of particle shape using X-ray tomography and spherical harmonics: Application to aggregates used in concrete. Cement Concrete Res 2002;32(10):1621–38.
[28] Wang LB, Frost JD, Lai JS. Three-dimensional digital representation of granular material microstructure from X-ray tomography imaging. J Comput Civil Eng 2004;18(1):28–35.
[29] Morris RJ, Najmanovich RJ, Kahraman A, et al. Real spherical harmonic expansion coefficients as 3D shape descriptors for protein binding pocket and ligand comparisons. Bioinformatics 2005;21(10):2347–55.
[30] Grigoriu M, Garboczi E, Kafali C. Spherical harmonic-based random fields for aggregates used in concrete. Powder Technol 2006;166(3):123–38.
[31] Liu X, Garboczi EJ, Grigoriu M, et al. Spherical harmonic-based random fields based on real particle 3D data: improved numerical algorithm and quantitative comparison to real particles. Powder Technol 2011;207(1–3):78–86.
[32] Garboczi EJ, Bullard JW. 3D analytical mathematical models of random star-shape particles via a combination of X-ray computed microtomography and spherical harmonic analysis. Adv Powder Technol 2017;28(2):325–39.
[33] Shen L, Makedon F. Spherical mapping for processing of 3D closed surfaces. Image Vision Comput 2006;24(7):743–61.
[34] https://www.med.upenn.edu/shenlab/spharm-mat.html.
[35] Zhou B, Wang JF, Zhao BD. Micromorphology characterization and reconstruction of sand particles using micro X-ray tomography and spherical harmonics. Eng geol 2015;184:126–37.
[36] Su D, Yan WM. 3D characterization of general-shape sand particles using microfocus X-ray computed tomography and spherical harmonic functions, and particle regeneration using multivariate random vector. Powder Technol 2018;323:8–23.
[37] Shi GH. Discontinuous deformation analysis: a new numerical model for the statics and dynamics of block system. Berkeley, California: University of California Berkeley; 1988.
[38] Fan H, He S. An angle-based method dealing with vertex–vertex contact in the two-dimensional discontinuous deformation analysis (DDA). Rock Mech Rock Eng 2015;48(5):2031–43.
[39] Fan H, Zheng H, Zhao JD. Discontinuous deformation analysis based on strain-rotation decomposition. Int J Rock Mech Min Sci 2017;92:19–29.
[40] Fan H, Zheng H, Wang JF. A generalized contact potential and its application in discontinuous deformation analysis. Comput Geotech 2018;99:104–14.
[41] Fan H, Zheng H, Zhao JD. Three-dimensional discontinuous deformation analysis based on strain-rotation decomposition. Comput Geotech 2018;95:191–210.
[42] Zhang YB, Xu Q, Chen GQ, et al. Extension of discontinuous deformation analysis and application in cohesive-frictional slope analysis. Int J Rock Mech Min Sci 2014;70:533–45.
[43] Peng XY, Yu PC, Zhang YB, et al. Applying modified discontinuous deformation analysis to assess the dynamic response of sites containing discontinuities. Eng Geol 2018;246:349–60.
[44] Yu PC, Zhang YB, Peng XY, et al. Evaluation of impact force of rock landslides acting on structures using discontinuous deformation analysis. Comput Geotech 2019;114:103–37.
[45] Peng XY, Chen GQ, Yu PC, et al. Improvement of joint definition and determination in three-dimensional discontinuous deformation analysis. Comput Geotech 2019;110:148–60.
[46] Mikola RG, Sitar N. Explicit three dimensional discontinuous deformation analysis for blocky system. In: 47th US Rock Mechanics/Geomechanics Symposium. American Rock Mechanics Association; 2013.
[47] Peng XY, Chen GQ, Yu PC, et al. Parallel computing of three-dimensional discontinuous deformation analysis based on OpenMP. Comput Geotech 2019;106:304–13.
[48] Fan H, Wang JF, Zheng H. Variational inequality-based particle discontinuous deformation analysis. Int J Numer Anal Methods Geomech. 2019;43:1995–2019.
[49] Hu SM, Wallner J. A second order algorithm for orthogonal projection onto curves and surfaces. Comput Aided Geom Des 2005;22(3):251–60.
[50] Zheng H, Zhang P, Du XL. Dual form of discontinuous deformation analysis. Comput Methods Appl Mech Eng 2016;305:196–216.
[51] Fan H, Zhao JD, Zheng H. Variational inequality-based framework of discontinuous deformation analysis. Int J Numer Methods Eng 2018;115(3):358–94.
[52] Fan H, Wang JF. Dynamic modeling of sphere, cylinder, done, and their assembly. Arch Comput Methods Eng 2019:1–48.
[53] Shi GH. Simplex integration for manifold method, FEM, DDA and analytical analysis. Proc. 1th Internat. Forum on Discontinuous Deformation Analysis, DDA and Simulations of Discontinuous Media. Albuquerque, New Mexico, USA: TSI Press; 1996. p. 205–62.
[54] He BS, Liao LZ. Improvements of some projection methods for monotone nonlinear variational inequalities. J Optim Theory Appl 2002;112:111–28.
[55] Hartmann E. On the curvature of curves and surfaces defined by normalforms. Comput Aided Geom Design 1999;16:355–76.
[56] van den Bergen G. Efficient collision detection of complex deformable models using AABB trees. J Graphics Tools 1997;2(4):1–14.
[57] Garboczi EJ, Bullard JW. Contact function, uniform-thickness shell volume, and convexity measure for 3D star-shaped random particles. Powder Technol 2013;237:191–201.
[58] Zhu Z, Chen H, Xu W, et al. Parking simulation of three-dimensional multi-sized star-shaped particles. Modell Simul Mater Sci Eng 2014;22(3):035008.
[59] Perram JW, Wertheim MS. Statistical mechanics of hard ellipsoids. I. Overlap algorithm and the contact function. J Comput Phys 1985;58(3):409–16.
[60] Qian Z, Garboczi EJ, Ye G, et al. Anm: a geometrical model for the composite structure of mortar and concrete using real-shape particles. Mater Struct 2016;49(1–2):149–58.
[61] Cundall PA. Formulation of a three-dimensional distinct element model Part I. A scheme to detect and represent contacts in a system composed of many polyhedral blocks. Int J Rock Mech Min Sci Geomech Abstr 1988;25:107–16.
[62] Nezami EG, Hashash YMA, Zhao D, et al. A fast contact detection algorithm for 3-D discrete element method. Comput Geotech 2004;31:575–87.
[63] Ting JM. A robust algorithm for ellipse-based discrete element modelling of granular material. Comput Geotech 1992;13:175–86.
[64] Lin XS, Ng TT. Contact detection algorithms for three-dimensional ellipsoids in discrete element modelling. Int J Numer Anal Methods Geomech 1995;19(9):653–9.
[65] https://www.codeproject.com/Articles/1065730/Point-Inside-Convex-Polygon-in-Cplusplus.
[66] Guilhem M, Zhao JD. 3D generation of realistic granular samples based on random fields theory and Fourier shape descriptors. Comput Methods Appl Mech Eng 2014;279:46–65.
[67] Dong LJ, Sun DY, Li XB, et al. Interval non-probabilistic reliability of surrounding jointed rockmass considering microseismic loads in mining tunnels. Tunn Undergr Space Technol 2018;81:326–35.
[68] Dong LJ, Shu WW, Li XB, et al. Quantitative evaluation and case studies of cleaner mining with multiple indexes considering uncertainty factors for phosphorus mines. J Clean Prod 2018;183:319–34.